ISPRS Journal of Photogrammetry and Remote Sensing 228 (2025) 489–504

Contents lists available at ScienceDirect

ISPRS Journal of Photogrammetry and Remote Sensing

journal homepage: www.elsevier.com/locate/isprsjprs

Mapping snow-covered forest albedo via hybrid radiative transfer and machine learning across Northern Hemisphere

Siyong Chen [a], Pengfeng Xiao [a,b,*], Xueliang Zhang [a], Petri Pellikka [c,d], Hao Liu [e], Yantao Liu [a]

[a] Jiangsu Provincial Key Laboratory of Geographic Information Science and Technology, Key Laboratory for Land Satellite Remote Sensing Applications of Ministry of Natural Resources, School of Geography and Ocean Science, Nanjing University, Nanjing, Jiangsu 210023, China
[b] Jiangsu Center for Collaborative Innovation in Geographical Information Resource Development and Application, Nanjing, Jiangsu 210023, China
[c] Department of Geosciences and Geography, University of Helsinki, Helsinki, Finland
[d] State Key Laboratory of Information Engineering in Surveying, Mapping and Remote Sensing, Wuhan University, Wuhan, Hubei 430000, China
[e] Department of Land Surveying and Geo-Informatics, The Hong Kong Polytechnic University, Hong Kong 999077, China

ARTICLE INFO

Keywords:
Snow-covered forests
Albedo
Radiative transfer
Random forest
Google Earth Engine

ABSTRACT

Snow-covered forests are widely distributed in the Northern Hemisphere, and their albedo significantly influences forest warming effects, radiative balance, and climate change. However, estimating snow-covered forest albedo is challenging due to the complex interactions between the snow and canopy. Current algorithms often rely on snow-free forest models or linear weighting of snow and forest components. These simplified forward models result in significant errors in the bidirectional reflectance simulation of snow-covered forests. Meanwhile, the albedo retrieval process is computationally intensive, especially when lookup tables or optimization algorithms are employed. Thus, we propose a novel albedo retrieval framework that integrates the strengths of snow-covered forest radiative transfer model with the efficiency of machine learning methods. This framework achieves three key advancements: (1) the snow-covered forest bidirectional reflectance (SFBR2) model is extended to sloped terrain to reduce the reflectance simulation errors; (2) the representativeness and accuracy of training datasets are improved by combining satellite observations with SFBR2-retrieved albedo; and (3) Random Forest model is utilized on the Google Earth Engine (GEE) platform to enable rapid retrieval of snow-covered forest albedo. As a result, a snow-covered forest albedo product for the Northern Hemisphere from 2001 to 2022 is successfully generated. Validation against albedo observations from flux stations demonstrates that our retrieval framework achieves higher accuracy ($R^2 \geq 0.775$ and RMSE ≤ 0.037) than the Moderate Resolution Imaging Spectroradiometer (MODIS) and Global LAnd Surface Satellites (GLASS) products. This highlights its potential to further enhance our understanding of radiative balance and climate change in snow-covered forests.

1. Introduction

More than one-fifth of snow-covered regions overlap with forests in the Northern Hemisphere (Rutter et al., 2009). The shielding of snow by forest canopies significantly reduces land surface albedo and exhibits a pronounced warming effect (Li et al., 2015), which further exacerbates global climate warming through albedo feedback (Kristensen et al., 2024). Changes in snow-covered forest albedo can also influence the timing of snowmelt, with cascading effects on vegetation photosynthesis and phenology (Bright et al., 2016; Wu et al., 2023). Therefore, obtaining accurate snow-covered forest albedo data is essential for improving climate change simulations and deepening our understanding of the feedback mechanisms between forests and snow cover (Bartlett and Verseghy, 2015). However, the complex interplay between the strong absorption of vegetation and high reflectivity of snow poses significant challenges in accurately quantifying snow-covered forest albedo (Manninen and Stenberg, 2009). Evaluations show that discrepancies in snow-covered forest albedo between land surface models and satellite products can exceed 50 % (Thackeray et al., 2015). Consequently, further studies on snow-covered forest albedo retrieval are urgently needed.

Parameter inversion requires the integration of effective forward

* Corresponding author.
E-mail address: xiaopf@nju.edu.cn (P. Xiao).

https://doi.org/10.1016/j.isprsjprs.2025.07.033
Received 18 February 2025; Received in revised form 16 July 2025; Accepted 22 July 2025

models and specific retrieval methods. For snow-covered forest scenarios, many models were developed to simulate the radiative transfer process. Photon recollision probability (Manninen and Stenberg, 2009), GeoSail (Klein et al., 1998), and the linear spectral mixing model (Bair et al., 2021; Vikhamar and Solberg, 2003) were established to simulate nadir reflectance or albedo. For bidirectional simulations, the zeroth-order radiative transfer model (Pulliainen et al., 2014) simulates the anisotropic reflection of coniferous forests under full snow cover via two-way canopy transmissivity. Wang et al. (2022) and Xin et al. (2012) coupled the geometric optical–radiative transfer (GORT) canopy model, snow radiative transfer model, and leaf property model to investigate the impact of anisotropic reflection characteristics on snow mapping in forested areas. In our previous study, the snow-covered forest bidirectional reflectance model (SFBR2) thoroughly considered the ground snow and soil coverage, needle leaf characteristics, anisotropic reflectivity of snow, and effects of canopy-intercepted snow (Chen et al., 2024), and demonstrated superior evaluation accuracy on flat terrain compared with unmanned aerial vehicle observations and three-dimensional radiative transfer modelling. However, albedo retrieval lags behind the progress of snow-covered forest models, and the aforementioned models have not been applied to enhance the accuracy of snow-covered forest albedo estimates.

Currently, albedo retrieval algorithms directly apply snow-free forest models or use linear weighting of snow and forest components for snow-covered forests, includes kernel-driven model, direct estimation algorithm, and optimization algorithm. The kernel-driven model was the core algorithm of the Moderate Resolution Imaging Spectroradiometer (MODIS) albedo (Schaaf et al., 2002) and GlobAlbedo (Lewis et al., 2012) products, and it fitted multiday cloud-free satellite reflectance via kernel functions (Lucht et al., 2000). This method, established based on the soil-canopy system, is unable to accurately simulate the anisotropic reflection characteristics of snow-covered forests. Direct estimation algorithm was successfully applied to Global LAnd Surface Satellites (GLASS) albedo product (Liang et al., 2013; Qu et al., 2014), which established the relationship between bidirectional reflectance and albedo via a kernel-driven model for snow-free surfaces and an asymptotic radiative transfer (ART) model (Kokhanovsky et al., 2011) for pure snow surfaces, and albedo retrieval was performed through lookup tables (He et al., 2018). However, the lookup table algorithm cannot balance both computational efficiency and accuracy simultaneously. Optimization algorithms were developed primarily for the synchronous retrieval of multiple surface parameters, including albedo (Ma et al., 2021; Zhang et al., 2022a), where a forward model was established by weighting PROSAIL (Jacquemoud et al., 2009) and ART with fractional snow cover to account for pixels that include snow-free and pure snow surfaces. This approach neglects the complex interactions between the canopy and snow. Moreover, this algorithm often involves a complex optimization process and leads to high computational demands (Zhang et al., 2022b). Although the above algorithms have made landmark contributions to albedo retrieval, their forward models fail to comprehensively represent the characteristics of snow-covered forests, and further improvements in computational efficiency are also needed.

The integration of radiative transfer with machine learning offers a new paradigm for retrieving land surface parameters (Ali et al., 2020; Verrelst et al., 2015), which simulates reflectance and target variables through a radiative transfer model to produce the training dataset, and performs parameter inversion via the machine learning method. For example, the PROSAIL model combined with Random Forest and Gaussian process regression have been used to retrieve the fractional vegetation cover, leaf area index (LAI), and grassland aboveground biomass (Estévez et al., 2020; Fernandez-Guisuraga et al., 2021; Xie et al., 2022); the soil–canopy–atmosphere radiative transfer model combined with Random Forest and Artificial Neural Networks has been applied to retrieve the LAI, FAPAR, and incident shortwave radiation (Shi et al., 2019). This method effectively balances the accuracy of forward models and the efficiency of retrieval methods (Zhang et al., 2022b, 2024).

Therefore, based on the insights from hybrid radiative transfer and machine learning, a novel albedo retrieval framework is proposed by combining the SFBR2 forward model with a Random Forest model to estimate snow-covered forest albedo. Considering that a robust forward model is essential for precise albedo retrieval, the SFBR2 model is further enhanced to account for sloped terrain by incorporating coordinate rotation and canopy gravitropism, significantly improving its reflectance simulation capabilities in complex mountainous regions. Building on the improved SFBR2 model and optimization algorithms, the training dataset is generated by combining satellite-observed reflectance and retrieved albedo to strengthen the sample representativeness and accuracy, which effectively avoids unrealistic angle combinations that might be simulated by radiative transfer models but fail to align with actual satellite observations. The well-trained Random Forest model is then employed for rapid retrieval of snow-covered forest albedo from MODIS reflectance data because it has strong adaptability, nonlinear processing capabilities, and is well integrated into the Google Earth Engine (GEE) platform. Moreover, a snow-covered forest albedo product for the Northern Hemisphere from 2001 to 2022 is generated, and field data from 9 flux stations are collected to validate the retrieved results.

2. Data and preprocessing

2.1. Satellite datasets for machine learning input

MODIS surface reflectance and elevation data are used to obtain input features for the machine learning methods. The MOD09GA product, available from 2001 to 2022, provides the daily surface reflectance for bands 1–7 at a 500-m resolution, along with the solar zenith/azimuth angle and viewing zenith/azimuth angle (Vermote et al., 2008). Specifically, these bands cover wavelengths ranging from 400 to 2500 nm: Band 1 (620–670 nm), Band 2 (841–876 nm), Band 3 (459–479 nm), Band 4 (545–565 nm), Band 5 (1230–1250 nm), Band 6 (1628–1652 nm), and Band 7 (2105–2155 nm). Quality control, cloud masking, and the MOD10A1 snow product are utilized to select high-quality snow pixels under cloud-free conditions. The elevation data are derived from the ASTER GDEM with a 100-m spatial resolution (Tachikawa et al., 2011). To match the MODIS reflectance data, the DEM data are resampled into 500-m grids for slope and aspect calculations. The MOD09GA, MOD10A1, and DEM products are available through the GEE platform (https://code.earthengine.google.com/).

2.2. Satellite products for comparison

The MODIS and GLASS albedo products are employed for comparison with the retrieved albedo data. MODIS products provide daily, 500-m shortwave black/white-sky albedo (BSA/WSA) from 2000 to present, retrieved via a kernel-driven model from MODIS surface reflectance (Schaaf et al., 2002). GLASS products provide 8-day, 1000-m shortwave BSA and WSA from 2000 to 2019, retrieved via direct estimation algorithms from the MODIS surface and top-of-atmosphere reflectance (Qu et al., 2014). When compared with field albedo, the actual (blue-sky) albedo is weighted by the BSA and WSA $\alpha = (1-\mathrm{SKYL})\alpha_{\mathrm{BSA}} + \mathrm{SKYL}\alpha_{\mathrm{WSA}}$, where SKYL is the fraction of diffuse skylight $\mathrm{SYKL} = 0.122 + 0.85e^{-4.8\cos(\theta_s)}$(Stokes and Schwartz, 1994) and θ_s is the solar zenith angle. The MODIS albedo products are available through the GEE platform, while the GLASS albedo products can be accessed from the official GLASS website (https://www.glass.hku.hk/).

2.3. Field data

Snow-covered forest albedo from flux stations are collected to validate the retrieved albedo (Table 1 and Fig. 1a). A total of 9 stations were

Table 1
Characteristics of the flux stations. DBF, ENF, and MF represent deciduous broadleaf forests, evergreen needleleaf forests, and mixed forests, respectively.

	Station ID	Stationname	Longitude (°)	Latitude (°)	Slope (°)	Aspect (°)	Forest type	Country	Temporal range	Number of field records
1	Ca1	British Columbia	−125.3336	49.8673	7	69	ENF	Canada	2001–2009	45
2	BK1	Bily Kriz forest	18.5369	49.5021	1	239	ENF	Czech Republic	2008–2014	53
3	Tha	Tharandt	13.5651	50.9626	2	88	ENF	Germany	2001–2014	48
4	Fmf	Flagstaff Managed Forest	−111.7273	35.1426	0	123	ENF	America	2006–2010	151
5	Hai	Hainich	10.4522	51.0792	3	9	DBF	Germany	2002–2005	6
6	Col	Collelongo	13.5881	41.8494	9	247	DBF	Italy	2005–2014	34
7	MMS	Morgan Monroe State Forest	−86.4131	39.3232	1	37	DBF	America	2002–2013	19
8	WCr	Willow Creek	−90.0799	45.8059	1	289	DBF	America	2001–2014	61
9	Cha	Changbaishan	128.0958	42.4025	3	88	MF	China	2003–2010	42

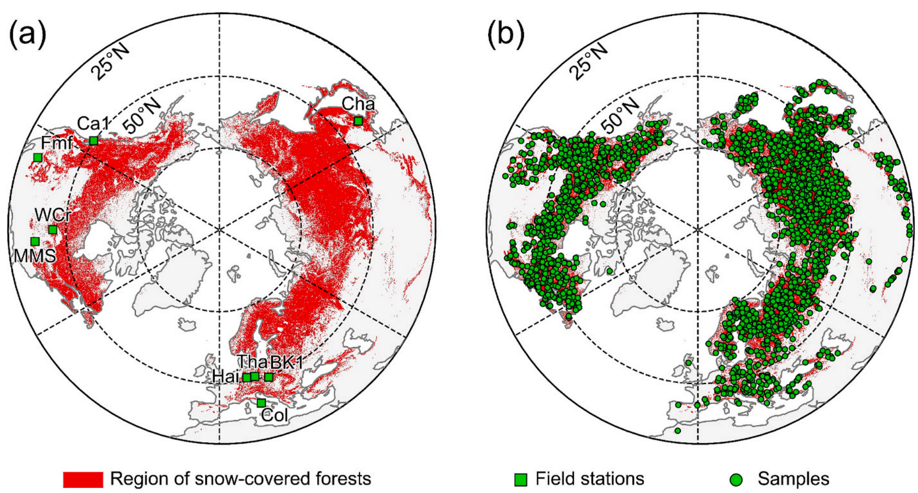

Fig. 1. Locations of field stations (a) and remotely sensed sampling sites (b) in snow-covered forests across the Northern Hemisphere.

selected based on stringent criteria for land cover homogeneity. Stations 1–8, obtained from the FLUXNET (https://fluxnet.org/) and AmeriFlux (https://ameriflux.lbl.gov/) networks, demonstrate good homogeneity at the 1000-m spatial scale on the basis of variogram estimation from Landsat ETM + images (Cescatti et al., 2012). Station 9, acquired from ChinaFlux (https://www.chinaflux.org/), also shows good homogeneity, as confirmed through field surveys and Google Earth imagery. All the stations record upwelling and downwelling shortwave radiation at 30-minute intervals. We calculate the shortwave albedo by taking the ratio of upwelling to downwelling shortwave radiation at the local solar noon and use it to validate the albedo retrieval results. The observed upwelling shortwave radiation at flux stations may include a portion of solar radiation under a large solar zenith angle, which introduces significant uncertainty into the field albedo (Wang et al., 2012); thus, we only use albedo measurements for validation when the solar zenith angle is below 75°. Moreover, field data with downwelling shortwave radiation greater than 400 W/m^2 are selected to ensure that the observed albedo represents clear-sky conditions. A total of 459 field records are ultimately collected.

2.4. Ancillary data

Land cover products from the European Space Agency Climate Change Initiative (CCI) projects (CCI, E.L.C., 2017) and snow water equivalent (SWE) products from ERA-5 land (Muñoz Sabater, 2019) are selected to identify the region of snow-covered forests. These products are obtained from the CEDA archive (https://data.ceda.ac.uk/) and the Copernicus Climate Data Store (https://cds.climate.copernicus.eu/), respectively. Forest extent is determined from the annual CCI land cover datasets (300-m resolution) for the period 2001–2020 by selecting areas with consistent forest types throughout the entire period. The selected forest types primarily include evergreen needleleaf, deciduous needleleaf, deciduous broadleaf, and mixed forests. The snow-covered region in the Northern Hemisphere is defined as areas where the average number of snow cover days exceeds one month, which can be identified via the daily 10-km ERA-5 land SWE product by the following steps: (1) binary snow cover maps are generated from the SWE products for the years 2001–2022 via a threshold of 2-mm (Zhong et al., 2021); (2) snow cover days are then calculated by summing the number of snow-covered pixels throughout the year; (3) pixels with average snow cover days of more than one month are extracted to represent the snow-covered regions. To ensure consistency with the MODIS reflectance data, the land cover and SWE products are resampled to a 500-m resolution using the nearest-neighbour method. The snow-covered forest region is then delineated by overlaying the forest extent with the snow-covered area (Fig. 1a). Given the seasonal variability of snow cover, the MOD10A1 product is additionally employed during the albedo retrieval process to identify daily snow cover conditions, ensuring that any uncertainties introduced by resampling do not significantly affect the final results. Additionally, the MOD44B fractional forest cover product (DiMiceli et al., 2015) for 2010 and the MOD10A1 normalized difference snow index (NDSI) product (Riggs et al., 2015) for November 2009, January 2010, and March 2010 are used to explore the albedo differences across different forest and snow conditions.

3. Methodology

3.1. Overview

A novel albedo retrieval framework for snow-covered forests is proposed by integrating forward models with machine learning methods (Fig. 2). The forward model is employed to accurately obtain albedo sample data corresponding to satellite-observed reflectance, while machine learning replaces the complex forward model to enable rapid large-scale albedo retrieval. Additionally, we optimized the radiative transfer process of the SFBR2 forward model for sloped terrain, allowing it to quantitatively simulate the bidirectional reflectance of snow-covered forests under varying sun-terrain-observation geometries. The entire retrieval process begins by collecting representative reflectance samples of snow-covered forests from MODIS observations. The SFBR2 model parameters are adjusted via an optimization algorithm to minimize the difference between the simulated reflectance and the MODIS surface reflectance. These optimized parameters are subsequently incorporated into the SFBR2 model to calculate the BSA and WSA. Finally, the reflectance and albedo data pairs are used as training samples for a machine learning method to generate snow-covered forest albedo products.

3.2. SFBR2 model for sloped terrain

The SFBR2 model is used to simulate the reflectance of snow-covered forests. This method effectively considers the proportional coverage of snow and soil on the ground, coniferous characteristics, canopy clumping effects, and canopy-intercepted snow. The SFBR2 model is coupled by ART snow model (Kokhanovsky et al., 2005), Walthall-BSM soil model (Nilson and Kuusk, 1989; Walthall et al., 1985; Yang et al., 2020), LIBERTY needleleaf model (Leblanc and Chen, 2000), 4SAIL2 canopy model (Verhoef and Bach, 2007), and canopy-intercepted snow model. Since snow-covered forests are widely distributed in mountainous areas, the SFBR2 model is further extended to sloped terrain in this study.

Accurately simulating terrain effects requires coordinate rotation from flat surface to sloped terrain and consideration of canopy gravitropism. The solar zenith/azimuth angle (θ_s/φ_s) is converted to the relative solar zenith/azimuth angle (θ_s'/φ_s') via rotation matrices (Shi and Xiao, 2021; Wu et al., 2018):

$$\begin{bmatrix} \sin\theta_s'\cos\varphi_s' \\ \sin\theta_s'\sin\varphi_s' \\ \cos\theta_s' \end{bmatrix} = \begin{bmatrix} \cos\alpha & 0 & -\sin\alpha \\ 0 & 1 & 0 \\ \sin\alpha & 0 & \cos\alpha \end{bmatrix} \begin{bmatrix} \cos\beta & \sin\beta & 0 \\ -\sin\beta & \cos\beta & 0 \\ 0 & 0 & 1 \end{bmatrix} \begin{bmatrix} \sin\theta_s\cos\varphi_s \\ \sin\theta_s\sin\varphi_s \\ \cos\theta_s \end{bmatrix} \tag{1}$$

where α and β are the slope and aspect, respectively. Similarly, the view zenith/azimuth angle (θ_v/φ_v) is converted to the relative view zenith/azimuth angle (θ_v'/φ_v'). Thus, the angles θ_s', φ_s', θ_v', and φ_v' are input into the ART snow model and Walthall-BSM soil model to simulate the reflection matrix of the land surface:

$$R^{\mathrm{l}} = \begin{bmatrix} r_{\mathrm{sd}}^{\mathrm{l}} & r_{\mathrm{dd}}^{\mathrm{l}} \\ r_{\mathrm{so}}^{\mathrm{l}} & r_{\mathrm{do}}^{\mathrm{l}} \end{bmatrix} = \mathrm{FSC}\begin{bmatrix} r_{\mathrm{sd}}^{\mathrm{snow}} & r_{\mathrm{dd}}^{\mathrm{snow}} \\ r_{\mathrm{so}}^{\mathrm{snow}} & r_{\mathrm{do}}^{\mathrm{snow}} \end{bmatrix} + (1-\mathrm{FSC})\begin{bmatrix} r_{\mathrm{sd}}^{\mathrm{soil}} & r_{\mathrm{dd}}^{\mathrm{soil}} \\ r_{\mathrm{so}}^{\mathrm{soil}} & r_{\mathrm{do}}^{\mathrm{soil}} \end{bmatrix} \tag{2}$$

where FSC is the fractional snow cover. The superscript “l” represents the land surface variables. r represents the reflectance, and these subscripts correspond to the direct solar (s), diffuse (d), and observer (o) fluxes.

The effects of canopy gravitropism involve converting leaf inclination and canopy clumping from flat to sloped terrain. Here, a spherical leaf inclination distribution was used to avoid incorrect leaf inclination corrections caused by coordinate rotation. Notably, when other leaf inclination distributions, such as erectophile, planophile, or plagiophile distributions, are used, it is necessary to remodel the leaf inclination distribution on the basis of the coordinate system for sloped terrain (Shi and Xiao, 2021). Canopy clumping was considered by the forest–light interaction model for flat terrain (Rosema et al., 1992). The projected canopy cover in the sunlit (C_s), view (C_o), and nadir (C_v) directions is represented as follows:

$$C_s = 1-(1-C_v)^{\frac{1}{\cos\theta_s}}C_o = 1-(1-C_v)^{\frac{1}{\cos\theta_o}}C_v = 1-e^{-\lambda\pi d^2} \tag{3}$$

where λ is the tree density for flat terrain and d is the tree radius. For sloped terrain, we provide similar projected canopy cover in the sunlit (C_s'), view (C_o'), and nadir (C_v') directions:

$$C_s' = 1-(1-C_v')^{\frac{1}{\cos\theta_s'}}C_o' = 1-(1-C_v')^{\frac{1}{\cos\theta_o'}}C_v' = 1-e^{-\lambda'\pi d^2} \tag{4}$$

where the tree density for flat and sloped terrain has the relationship $\lambda' = \lambda\cos(\alpha)$ (Wu et al., 2018); thus, we can derive the following equation:

$$C_s' = 1-(1-C_v)^{\frac{\cos\alpha}{\cos\theta_s'}}C_o' = 1-(1-C_v)^{\frac{\cos\alpha}{\cos\theta_o'}} \tag{5}$$

The areas of the sunlit canopy (F_{cs}'), sunlit floor (F_{os}'), shaded canopy (F_{cd}'), and shaded floor (F_{od}') for sloped terrain can be acquired:

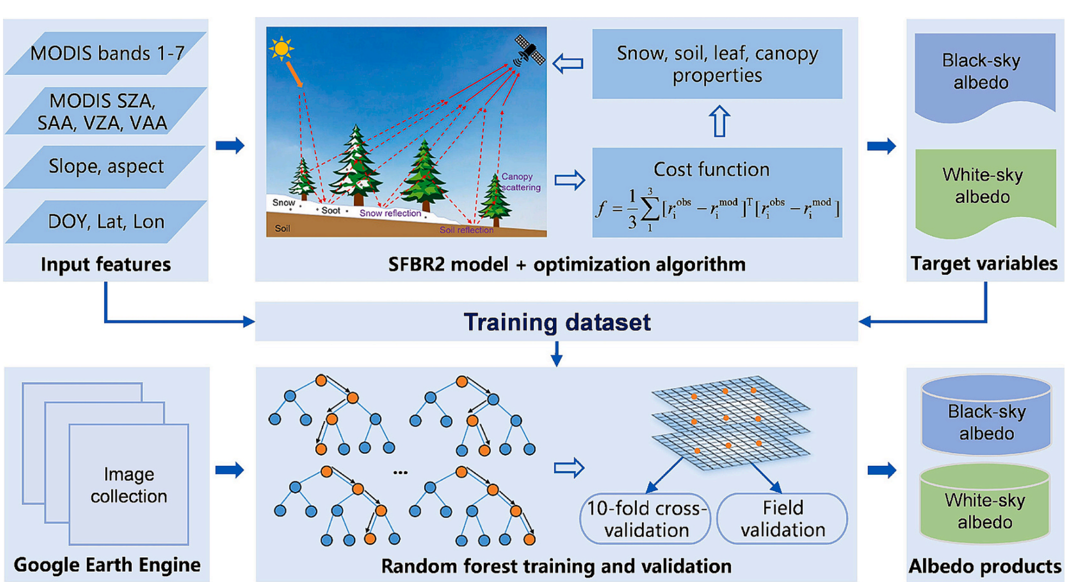

Fig. 2. Flowchart of snow-covered forest albedo retrieval.

$$F_{cd}' = C_s'C_o' + O'F_{cs}' = C_o'(1 - C_s') - O'F_{od}' = C_s'(1 - C_o') - O'F_{os}' = (1 - C_s')(1 - C_o') + O' \quad (6)$$

where

$$O' = \min[C_s'(1 - C_o'), C_o'(1 - C_s')]e^{\frac{-\xi' h}{2d}} \quad (7)$$

$$\xi' = \sqrt{\tan^2\theta_s' + \tan^2\theta_o' - 2\tan\theta_s'\tan\theta_o'\cos\psi} \quad (8)$$

where h represents the vertical distance from the ground to the center of the crown and ψ is the relative azimuth angle.

Furthermore, we input the reflectance/transmittance of leaves, the reflectance/transmittance of canopy-intercepted snow, the relative solar zenith/azimuth angle, and the relative view zenith/azimuth angle into the 4SAIL2 model. The clumping effects of the canopy are effectively considered, and the scattering matrix of the canopy for sloped terrain can be obtained.

$$\begin{bmatrix} T_d^c & R_b^c \\ R_t^c & T_u^c \end{bmatrix} == \begin{bmatrix} \tau_{ss}^c & 0 & 0 & 0 \\ \tau_{sd}^c & \tau_{dd}^c & \rho_{dd}^c & 0 \\ \rho_{sd}^c & \rho_{dd}^c & \tau_{dd}^c & 0 \\ \rho_{so}^c & \rho_{do}^c & \tau_{do}^c & \tau_{oo}^c \end{bmatrix} = \begin{bmatrix} C_s'\tau_{ss}^{c'} + (1 - C_s') & 0 & 0 & 0 \\ C_s'\tau_{sd}^{c'} & C_v\tau_{dd}^{c'} + (1 - C_v) & C_v\rho_{dd}^{c'} & 0 \\ C_s'\rho_{sd}^{c'} & C_v\rho_{dd}^{c'} & C_v\tau_{dd}^{c'} + (1 - C_v) & 0 \\ (1 - F_{os}')\rho_{so}^{c'} & C_o'\rho_{do}^{c'} & C_o'\tau_{do}^{c'} & C_o'\tau_{oo}^{c'} + (1 - C_o') \end{bmatrix} \quad (9)$$

where R and ρ represent the reflectance matrices and the corresponding values, respectively, and T and τ represent the transmittance matrices and the corresponding values, respectively. The parameters with superscripts c and c' indicate that the canopy considered clumping effects and was not considered. In the left matrix, the subscripts denote the downwards (d), upwards (u), top (t), and bottom (b) components. Note that $\tau_{ss}^c\tau_{oo}^c$ needs to be replaced with $\tau_{ssoo}^c = F_{cd}'\tau_{ssoo}^{c'} + F_{cs}'\tau_{oo}^{c'} + F_{od}'\tau_{ss}^{c'} + F_{os}'$ because it better accounts for the canopy shadowing effects (Niu et al., 2022).

The interaction between the land surface and canopy is simulated via four-stream theory (Verhoef et al., 2007). By inputting the surface reflectance R^l and the scatter matrix of the canopy R_t^c, R_b^c, T_d, and T_u^c, we can derive the expression for the reflection matrix at the top of the canopy:

$$R^c = \begin{bmatrix} r_{sd}^c & r_{dd}^c \\ r_{so}^c & r_{do}^c \end{bmatrix} = R_t^c + T_u^c[I - R_b^c R^l]^{-1} R^l T_d \quad (10)$$

At the bottom of the atmosphere, the reflectance observed by satellites includes direct and diffuse fluxes. Thus, the surface reflectance is weighted by SKYL:

$$r = \frac{r_{so}^c F_{sun} E_{dir} + r_{do}^c F_{sky} E_{dif}}{F_{sun} E_{dir} + F_{sky} E_{dif}} = \frac{r_{so}^c F_{sun}(1 - \mathrm{SKYL}) + r_{do}^c F_{sky}\mathrm{SKYL}}{F_{sun}(1 - \mathrm{SKYL}) + F_{sky}\mathrm{SKYL}} \quad (11)$$

where

$$F_{sun} = \Theta\frac{\cos\theta_s'}{\cos\theta_s}, F_{sky} = s\frac{\cos\theta_s'}{\cos\theta_s} + (1 - s)V_{sky} \quad (12)$$

where F_{sun} and F_{sky} are the corresponding correction factors for sloped terrain. Θ is a binary coefficient that is equal to one for sunlit pixels and zero for shaded pixels. F_{sky} is weighted by isotropic and anisotropic circumsolar diffuse components, and s is an anisotropy index that can be a substitute for direct atmospheric transmittance (Mousivand et al., 2015). In this study, the isotropic diffuse radiation assumption was adopted to facilitate calculation. V_{sky} is the proportion of diffuse radiation unobstructed by the surrounding topography in hemispherical space (Jeff and James, 1990), and many analytical algorithms can calculate this factor accurately on the basis of the DEM (Jiao et al., 2019b). When the DEM is unavailable, the trigonometric method is widely used for approximation calculations $V_{sky} = (1 + \cos\alpha)/2$ (Liu and Jordan, 1960).

3.3. Training dataset generation

The core idea of this study is to combine radiative transfer models and machine learning methods for snow-covered forest albedo retrieval. Therefore, the representativeness and accuracy of the training dataset directly impact the final product's accuracy. The input features of the samples are selected from MODIS observations in the region of snow-covered forest to ensure sample representativeness. Moreover, the albedo retrieved by the SFBR2 and optimization algorithms ensures the accuracy of the target variables.

There are several rules for selecting representative MODIS reflectance data for radiative transfer model-based retrieval: (1) the selected MODIS reflectance data are exclusively from the representative years of 2005, 2010, 2015, and 2020; (2) 2,000 locations are randomly generated within region of snow-covered forests (Fig. 1b), with different locations each year; (3) the selected MODIS reflectance data are cloud-free, high quality, and snow-covered for three consecutive days; and (4) only one MODIS reflectance data per location is retained each month to reduce data redundancy. Overall, we obtained 17,498 MODIS reflectance data from three consecutive days of clear-sky observations, including MODIS bands 1–7, solar zenith/azimuth angle (SZA/SAA), view zenith/azimuth angle (VZA/VAA), and their corresponding slope, aspect, day of year (DOY), longitude (Lon), and latitude (Lat). The last three features are primarily used to calculate the solar zenith angle at noon, ensuring that the final retrieved albedo values correspond to noon rather than the overpass time.

Determining the sensitive parameters of the forward model is a crucial step in performing optimization inversion. Our previous study carried out a sensitivity analysis for the SFBR2 model in seven MODIS bands based on the extended Fourier amplitude sensitivity testing (EFAST) method (Saltelli et al., 1999), which clearly revealed that the FSC, C_v, B, a_{ef}, C_{soot}, TAI, Diss, F_{cis}, SMC, X_u, Diameter, C_w, and C_{ab} have the highest total-order sensitivity indices, indicating that these parameters are the most sensitive in affecting reflectance (Chen et al., 2024). Thus, we set these as free parameters, and other parameters were set to default values.

Furthermore, we ran the optimization algorithm for the selected MODIS observations to retrieve the BSA and WSA, which adjusted the parameters of snow-covered forests iteratively to minimize a cost function:

$$f = \frac{1}{3}\sum_1^3 [r_i^{obs} - r_i^{mod}]^T [r_i^{obs} - r_i^{mod}] \quad (13)$$

where r_i^{obs} represents the reflectance observed by the MODIS sensor on the ith day and r_i^{mod} represents the corresponding reflectance simulated by SFBR2. The optimization algorithm operates with the following steps: (1) the default parameters are input into the SFBR2 model to simulate surface reflectance; (2) the cost function is optimized via the minimize function in Python's SciPy library, which adjusts the sensitive parameters within their valid ranges to find the optimal solution, and the specific parameter ranges are referenced from our previous study (Chen et al., 2024); and (3) the optimized parameters are subsequently fed into the SFBR2 model to simulate the BSA and WSA. The input and output variables from optimization algorithms are combined to generate the training dataset. It should be noted that the machine learning model utilized only clear-sky MODIS reflectance for albedo retrieval, with each sample containing 16 input features (MODIS bands 1–7, solar zenith/azimuth angle, sensor zenith/azimuth angle, slope, aspect, day of year, longitude, and latitude) and 2 target variables (BSA and WSA).

3.4. Albedo retrieval via Random forest model

We utilized a Random Forest model to retrieve the BSA and WSA from MODIS surface reflectance data on the GEE platform. Unlike radiative transfer models, which define a mapping function for inputs and outputs, Random Forest establishes complex nonlinear relationships between input features and target variables by combining multiple decision trees. It has the distinct advantages of having fewer hyperparameters, not requiring normalization, and being insensitive to collinearity between input features, which results in outstanding performance in biophysical parameter retrieval and land surface classification within the remote sensing community (Bao et al., 2023; Luan et al., 2022).

The process for retrieving snow-covered forest albedo via the Random Forest model in GEE consists of the following steps. First, we collected the required input features and target variables to train the Random Forest model. A grid search algorithm was used to optimize the hyperparameters, specifically the number of decision trees (Ntree) and the maximum number of features (Mtry). The 10-fold cross-validation was used to evaluate the effectiveness of the trained model, with the optimal hyperparameters selected based on the highest coefficient of determination (R^2). Second, MODIS reflectance, DEM, and other datasets were integrated to construct a long-term time series image collection with 16 input features, to which the trained Random Forest model was then applied to retrieve snow-covered forest albedo. Finally, the BSA and WSA of snow-covered forests in the Northern Hemisphere were efficiently generated from 2001 to 2022.

4. Results

4.1. Accuracy of training dataset and machine learning methods

The accuracy of the albedo in the training samples directly influences the precision of the final albedo retrieval. In this study, albedo samples are generated using three consecutive days of clear-sky MODIS reflectance data and a radiative transfer model. Accordingly, only field albedo measurements that satisfied the same clear-sky condition can be used for validation, resulting in 85 field samples. We evaluate the quality of the albedo in the training samples by comparing the SFBR2-based albedo with field measurements. Additional comparisons are made with the ART snow model, the PROSAIL snow-free forest model, and the SFBR2 model without considering topographic effects (Fig. 3). ART model tend to overestimate the snow-covered forest albedo, particularly when the field albedo is less than 0.18 (Fig. 3a). These significant biases can be attributed to the fact that the ART model is designed primarily for highly reflective snow and fails to account for the canopy's shading effect. In contrast, the PROSAIL model shows discrepancies when the field albedo exceeds 0.18, with some overestimations and some underestimations (Fig. 3b). This is likely due to highly reflective snow altering the radiative properties of forests, and the PROSAIL model lacks the ability to simulate the reflective properties of snow components. Compared with

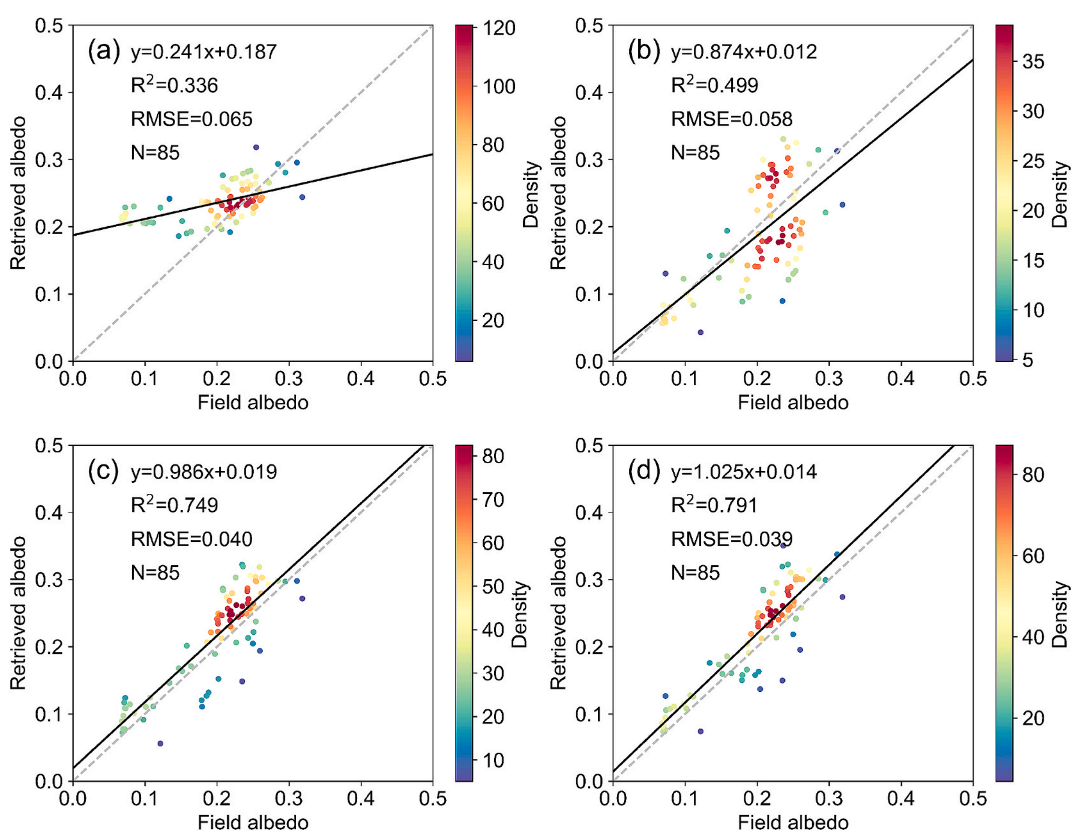

Fig. 3. Comparison of retrieved results by ART (a), PROSAIL (b), SFBR2 without sloped terrain consideration (c), and SFBR2 with sloped terrain consideration (d), against field albedo in snow-covered forests.

the ART and PROSAIL models, the albedo retrieved by the SFBR2 model shows better consistency with the field values (Fig. 3c). This is because the SFBR2 model accounts for fractional snow cover on land, discontinuous canopy distributions, and the characteristics of canopy-intercepted snow (Chen et al., 2024). In this study, we extend the SFBR2 model to sloped terrain and achieve the highest albedo retrieval accuracy, with an R^2 of 0.791 and a root mean squared error (RMSE) of 0.039 (Fig. 3d), which clearly demonstrates the reliability of the retrieved albedo samples.

Furthermore, both the Random Forest and the Artificial Neural Network models were quantitatively evaluated using 10-fold cross-validation. On the basis of the grid search algorithm, the optimal hyperparameters for the Random Forest were determined to be 100 for Ntree and 0.2 for Mtry. The optimal hyperparameters for the Artificial Neural Network were determined: one hidden layer, a hidden layer size of 20, the ReLU activation function, the ADAM solver, a learning rate of 0.1, and a maximum number of iterations of 500. Using these optimal settings, Fig. 4 shows the results of the 10-fold cross-validation based on the training dataset. The estimation accuracy of the Random Forest model is similar to the results of Artificial Neural Network, with an R^2 exceeding 0.852 and an RMSE below 0.052. This finding indicates that the choice of machine learning method has a minimal effect on the retrieval accuracy for snow-covered forest albedo. Given GEE's computational efficiency and its built-in support for the Random Forest model, we applied it to retrieve snow-covered forest albedo in our study.

The relative importance of input features in albedo retrieval is quantitatively assessed through SHAP (SHapley Additive exPlanations) analysis, with features ranked according to their mean absolute SHAP values (Lundberg and Lee, 2017). As illustrated in Fig. 5, spectral bands 1–5 consistently demonstrate the strongest predictive power for albedo estimation, while bands 6–7 exhibit comparatively lower importance. Notably, band 3 emerges as the most influential predictor for BSA retrieval, exhibiting the highest SHAP values. This finding corroborates previous studies on narrowband-to-broadband albedo conversion, where band 3 is consistently assigned the highest weight coefficient (Stroeve et al., 2005). Among the geometric parameters, the solar zenith angle shows greater influence on BSA than on WSA. This differential impact aligns with fundamental radiative transfer theory, as BSA is calculated by integrating radiance over the observation hemisphere only, whereas WSA represents a hemispherical integration over both incident and observation directions (Qu et al., 2015). Terrain-related factors demonstrate relatively limited influence on snow-covered forest albedo in our analysis, which likely stems from the comprehensive Northern Hemisphere coverage of our dataset, which is predominantly characterized by flat terrain. However, terrain effects are markedly enhanced in mountainous regions due to pronounced topographic complexity that generates local variations in surface orientation and shadowing (Hao et al., 2019; Weiser et al., 2016).

4.2. Albedo validation via field measurements

Flux measurements from 9 stations collected over multiple years under clear-sky conditions are utilized to estimate the albedo of snow-covered forest areas. The retrieved albedo that considers topographic effects compares well with the field data, with R^2 values of 0.818 and RMSE values of 0.037 (Fig. 6). If topographic effects are ignored, the correlations between the retrieved albedo and field values degrade considerably, with R^2 values of 0.809 and RMSE values of 0.038. At different field stations and during different months, the difference between the retrieved results that consider topographic effects and the field measurements is closer to zero than the results without considering topographic effects. This finding is consistent with the results shown in Fig. 3, all indicating that considering topographic effects can further enhence the retrieval accuracy of snow-covered forest albedo.

The MODIS and GLASS products are also compared with our retrieved results. The daily results for our retrieval and MODIS products are presented in Fig. 6. Based on the hybrid radiative transfer and machine learning retrieval framework, our results achieved better

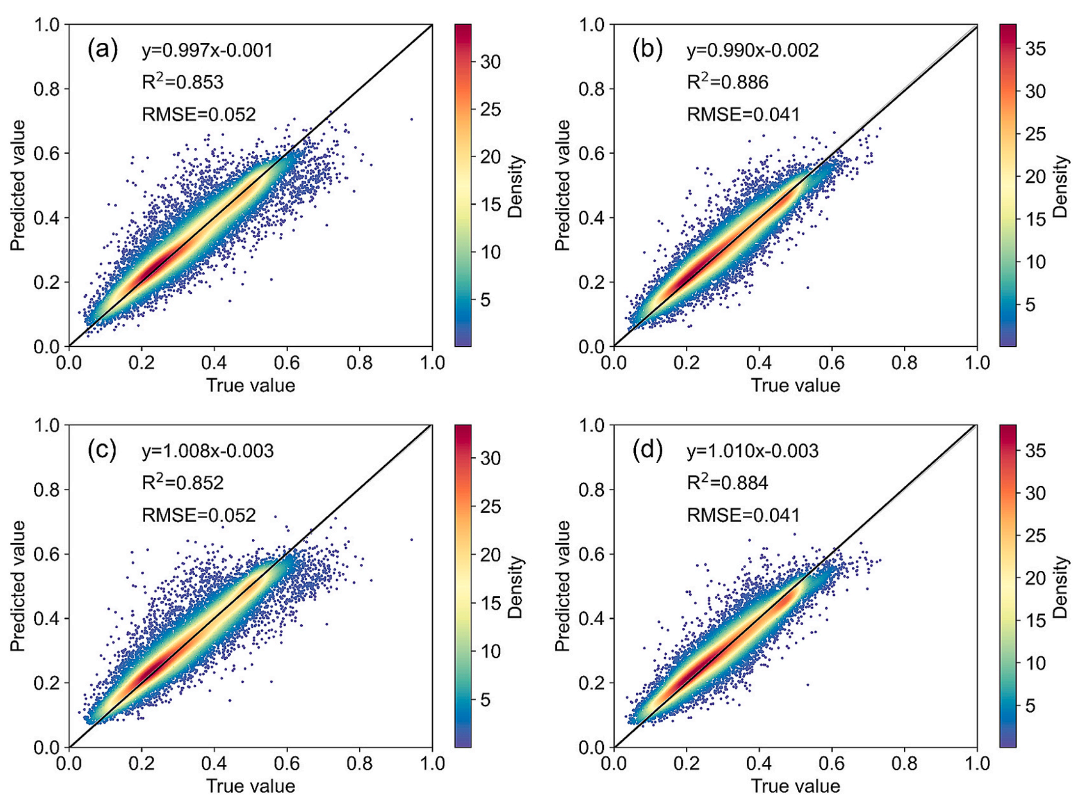

Fig. 4. Accuracy of the training dataset based on 10-fold cross-validation for the BSA (a) and WSA (b) via the Artificial Neural Network and for the BSA (c) and WSA (d) via the Random Forest.

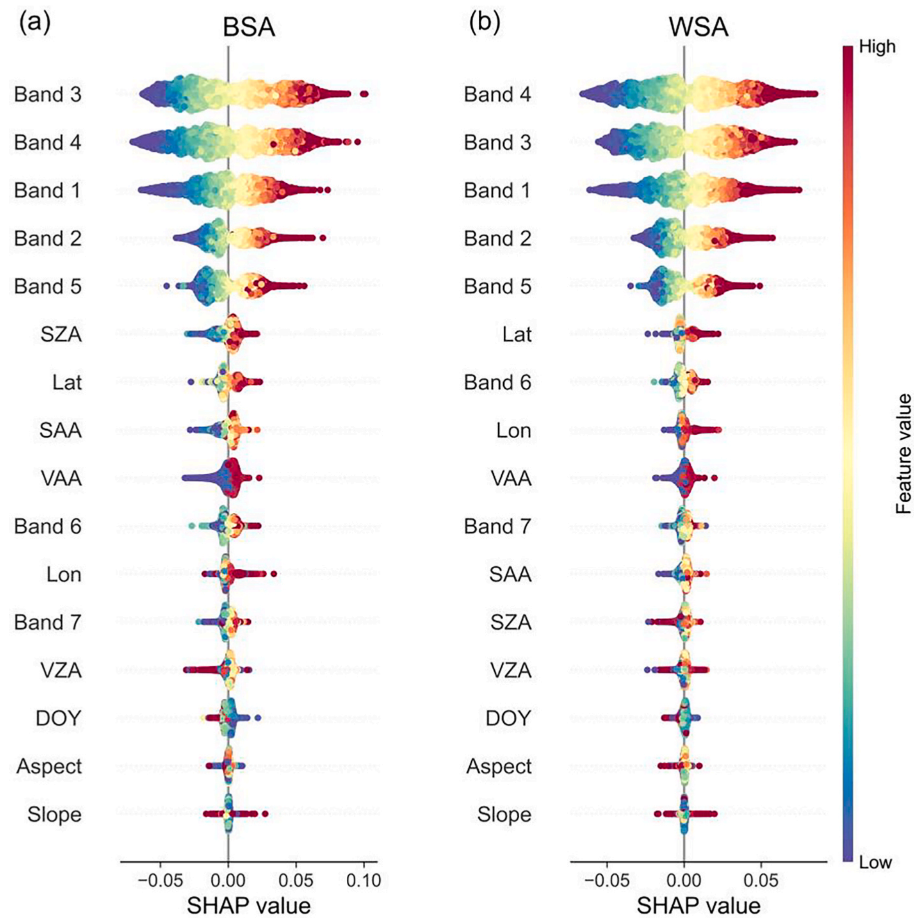

Fig. 5. Relative importance and marginal contributions (SHAP values) of multiple variables to BSA and WSA.

accuracy, with R^2 improved from 0.747 to 0.818 and the RMSE decreased from 0.056 to 0.037 compared with the MODIS product. At each field station, our results exhibited a slight overestimation with mean values between 0.009 and 0.043, whereas the MODIS product showed larger discrepancies with mean values between –0.044 and 0.061. From a monthly perspective, our retrieved results (mean values: 0.009–0.026) also outperformed the MODIS product (mean values: –0.011–0.061). This is largely because the kernel-driven model used in the MODIS product struggles to capture the forward scattering properties of snow (Jiao et al., 2019a), impacting the precision of snow-covered forest albedo retrieval.

The validation of the 8-day composite snow-covered forest albedo products and the GLASS products is shown in Fig. 7. Our results improved the retrieval accuracy with R^2 increasing from 0.443 to 0.775 and the RMSE decreasing from 0.047 to 0.036 compared with the GLASS product. Similarly, the individual station and monthly results further demonstrated that our retrieval outperforms the GLASS product. This is because the GLASS product builds a training dataset based on vegetation, snow, bare ground, and their mixed types to drive a direct estimation algorithm (Liu et al., 2013; Qu et al., 2014), without adequately considering the structure and reflective properties of snow-covered forests in the forward model. Overall, the comparisons clearly confirm that our method can accurately retrieve snow-covered forest albedo and the retrieved results effectively capture the forest albedo changes caused by snow.

Furthermore, the interannual performance of the retrieved, MODIS, and GLASS albedo products is comprehensively evaluated using field observations from nine stations (Fig. 8). Among the three products, the retrieved albedo consistently shows the highest agreement with in-situ measurements, with an R^2 of 0.792 and an RMSE of 0.032. Particularly strong performance is observed at stations BK1, Fmf, Col, MMS, and WCr, where it yields the lowest RMSE across all products, with values below 0.023. In contrast, the MODIS and GLASS products tend to exhibit greater biases and inconsistent interannual variability, likely due to their 16-day compositing strategies and spatiotemporal smoothing processes, which are not well suited to capturing rapid changes in snow cover. The MODIS product shows an R^2 of 0.687 and an RMSE of 0.038, whereas GLASS presents a lower R^2 of 0.509 and an RMSE of 0.036. Although MODIS performs best at the Hai station, the limited record of only four years undermines its statistical significance. Similarly, GLASS outperforms the other products at the Tha station; however, all three products exhibit nearly identical temporal trends, with RMSE differences within 0.006. This interannual analysis highlights the effectiveness of the retrieval approach in preserving interannual variability and providing a more physically consistent estimate of snow-covered forest albedo.

4.3. Consistency and difference analysis relative to other products

Clarifying the consistency and differences between the retrieved, MODIS, and GLASS albedos is crucial for their application. We primarily compare the BSA in this study because it shows good correlation with the WSA (Alibakhshi et al., 2020). The monthly composite results for November 2009, January 2010, and March 2010 in the Northern Hemisphere are used for comparison, and 3,687 sample points are randomly selected for consistency evaluation. Overall, the three products exhibit similar spatial distributions (Fig. 9a–c). The retrieved BSA is more consistent with the MODIS product, with R^2 greater than 0.801 and RMSE less than 0.090 (Fig. 10a–c). The consistency between the retrieved BSA and the GLASS product is significantly lower than that

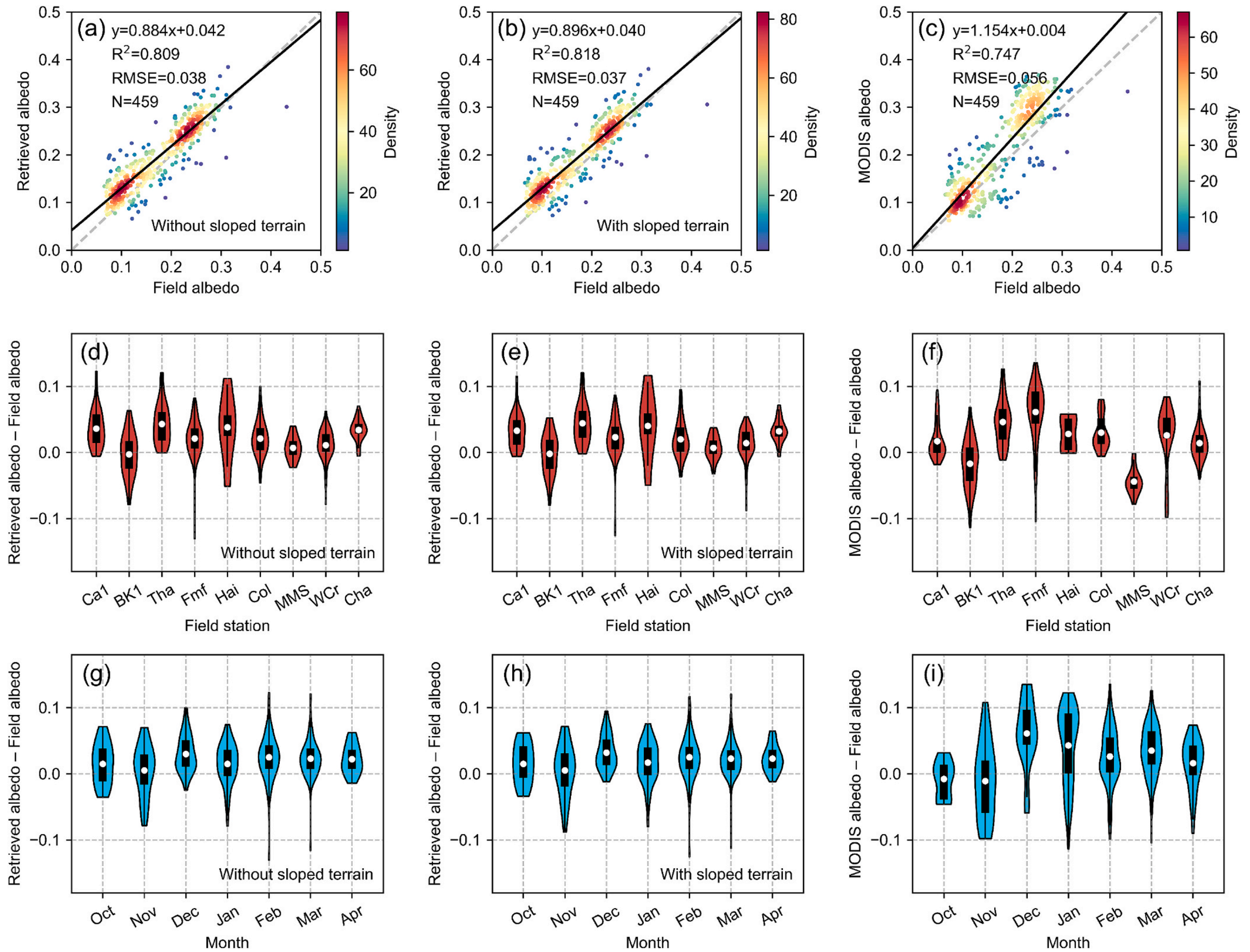

Fig. 6. Validation of daily snow-covered forest albedo based on field measurements. Panels (a), (d), and (g) show the comparison of retrieved albedo (without slope terrain consideration) and field albedo, and their differences at different flux stations and across months. Panels (b), (e), and (h) show the comparison of retrieved albedo (with slope terrain consideration) and field albedo, and their differences at different flux stations and across months. Panels (c), (f), and (i) show the comparison of MODIS and field albedo, and their differences at different flux stations and across months.

with the MODIS product, with R^2 greater than 0.354 and RMSE less than 0.121 (Fig. 10d–f). Moreover, the correlations between the retrieved BSA and MODIS, as well as the retrieved BSA and GLASS, also exhibited similar accuracies across different months.

The differences between the retrieved results and the MODIS products, as well as GLASS products, in the Northern Hemisphere for January 2010 are shown in Fig. 9d–e. Overall, the retrieved BSA is slightly lower than the MODIS product, with differences primarily concentrated in the range of –0.1 to 0. In contrast, the discrepancies with the GLASS products are larger than those with the MODIS products, which aligns with the field validation results in Fig. 6 and Fig. 7. Additionally, we examined the differences between our retrieved results and the MODIS and GLASS products across varying fractional forest cover and NDSI values in November 2009, January 2010, and March 2010 (Fig. 11). As the fractional forest cover decreases and the NDSI increases, the mean difference between our retrieved results and the MODIS product gradually decreases from –0.003 to –0.095. The pronounced discrepancies observed under conditions of low fractional forest cover and high NDSI values can be primarily attributed to the inherent limitations of the kernel-driven model in precisely characterizing snow anisotropy. However, for the GLASS product, the mean differences remain close to zero across varying fractional forest cover and NDSI conditions, likely because the GLASS product also employs a snow radiative transfer model, thus avoiding any systematic over- or under-estimation.

4.4. Generating Northern Hemisphere estimates

We generated daily snow-covered forest albedo data from 2001 to 2022 via the trained Random Forest model. Furthermore, the 500-m daily products were aggregated into 25-km monthly albedo datasets to enable more convenient spatiotemporal analyses across the Northern Hemisphere. This aggregation not only removes cloud pixels but also alleviates the data processing burden for large-scale analysis. The BSA effectively captures variations in surface reflection characteristics without interference from atmospheric disturbances; thus, BSA products from the retrieved, MODIS, and GLASS were used for analysis in this study.

The spatial patterns of snow-covered forest albedo throughout the whole year, as well as during the snow accumulation, stable, and melt periods, are shown in Fig. 12. Overall, our retrieved, MODIS, and GLASS product exhibit similar spatial distribution patterns. Snow-covered forest albedo in the Northern Hemisphere ranges from 0 to 0.6, with a mean value of 0.336. Albedo generally increases with latitude, and values in eastern Siberia are notably higher than those in other regions. This is attributed to the greater snow cover at higher latitudes (Bormann et al., 2018; Pulliainen et al., 2020) and the significantly lower forest coverage

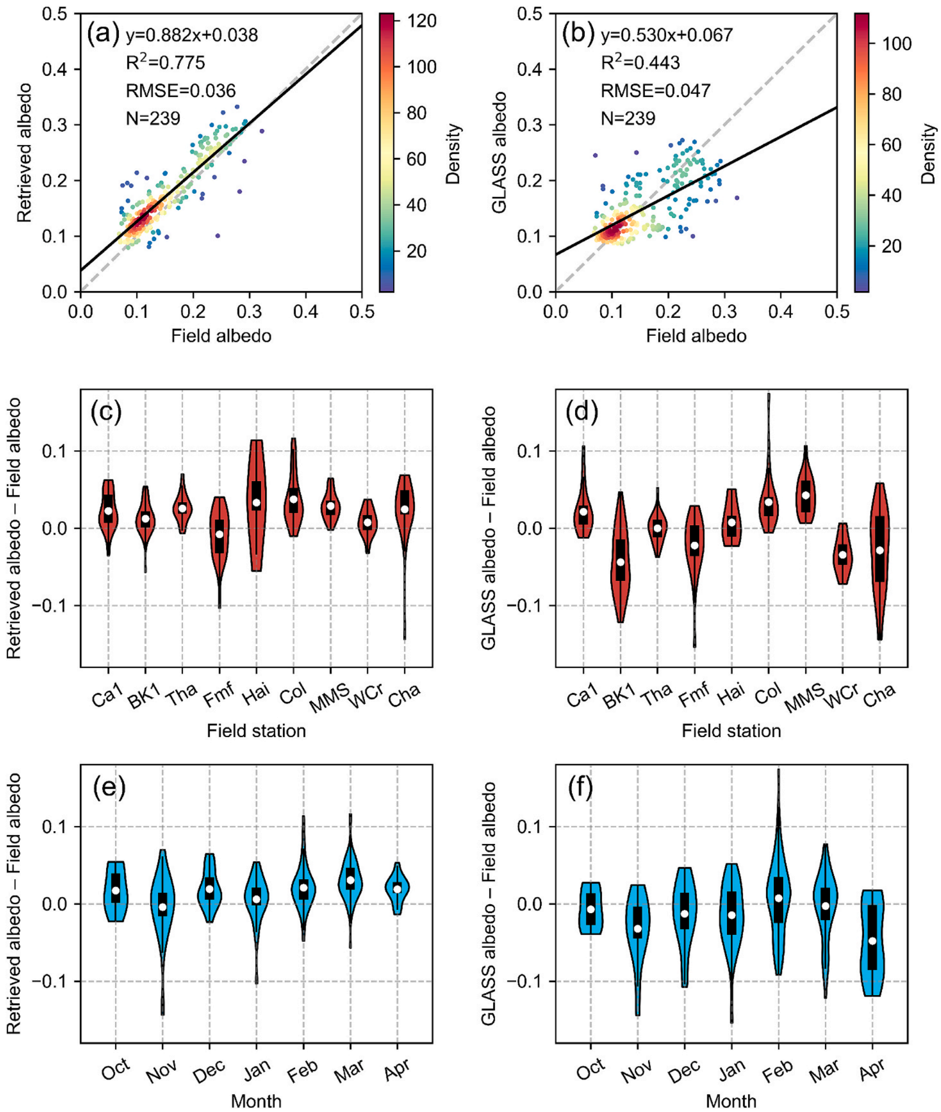

Fig. 7. Validation of 8-day composite snow-covered forest albedo based on field measurements. Panels (a), (c), and (e) show the comparison of retrieved albedo with field albedo, and their differences at different flux stations and across months. Panels (b), (d), and (f) show the comparison of GLASS albedo with field albedo, and their differences at different flux stations and across months.

in East Siberia than in other areas (Loranty et al., 2014). Across different snow periods, albedo is significantly higher during stable periods than during accumulation and melt periods, as snow cover is typically greatest in winter (Brutel-Vuilmet et al., 2013). However, some seasonal differences are also evident for different products. For instance, during the snow accumulation period, the GLASS albedo is significantly higher than that of our product and MODIS. And during the snowmelt period, our retrieved albedo is slightly lower than that of MODIS and GLASS. These discrepancies are mainly attributed to the different assumptions regarding snow-covered forests embedded in the retrieval algorithms.

The trend of snow-covered forest albedo was evaluated via the modified Mann-Kendall test (Hamed and Rao, 1998) and Theil-Sen median slope (Sen and Kumar, 1968). Fig. 13 shows significant slope changes with a p-value less than 0.05. For the interannual trend, our retrieved results indicate that 9.38 % of snow-covered forest areas exhibit a significant decreasing trend, primarily located in the Central Siberia and Eastern European Plain, whereas 8.28 % show a significant increasing trend, mainly in southwestern Canada. The slope of snow-covered forest albedo changes is predominantly within the range of –0.003 to 0.003 (Fig. 13a), which closely aligns with the trend observed during the snow stable period (Fig. 13c), indicating that the stable period plays a decisive role in albedo changes over the whole year. During the snow accumulation period, only 7.88 % of the snow-covered forest areas show significant albedo changes (Fig. 13b), with a predominant increasing trend observed in North America and Central Siberia. This is likely due to the reduction in forest cover, which leads to enhanced snow exposure and consequently increases the surface albedo (Wang and Shi, 2020). During the snowmelt period, albedo changes are characterized primarily by a decreasing trend (12.22 %), particularly in Asia (Fig. 13d). This trend may be linked to an earlier snow end date (Chen et al., 2015), as reduced snow cover leads to a decrease in snow-covered forest albedo. The MODIS product demonstrates a trend pattern that is generally consistent with our retrieved results (Fig. 13e–h). In contrast, the GLASS product exhibits a more pronounced and persistent decreasing trend in albedo across all snow periods (Fig. 13i–l). This divergence may stem from the 8-day compositing approach employed in GLASS (Liu et al., 2013), which could introduce albedo values from snow-free forest conditions into the final dataset. As a result, the GLASS product may not accurately reflect the true variations in albedo associated with snow-covered forest regions.

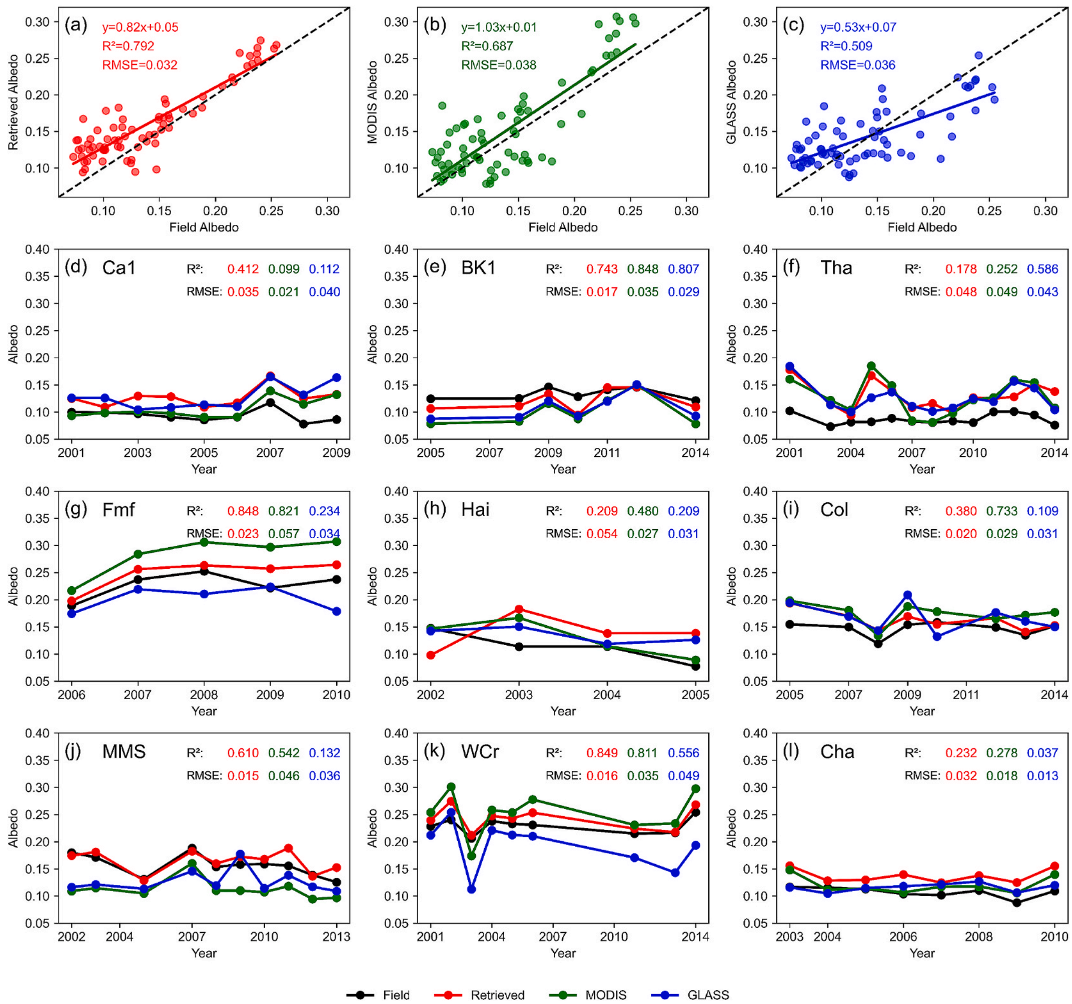

Fig. 8. Interannual consistency between retrieved, MODIS, and GLASS albedo products and field measurements.

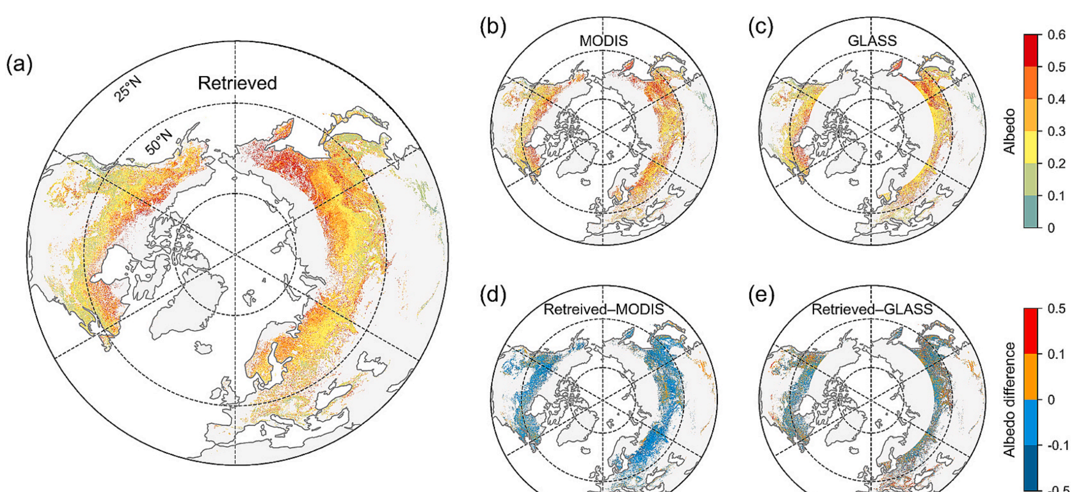

Fig. 9. Comparison of the retrieved snow-covered forest albedo with MODIS and GLASS products across the Northern Hemisphere for January 2010: (a) retrieved BSA; (b) MODIS BSA; (c) GLASS BSA; (d) difference between retrieved BSA and MODIS BSA; and (e) difference between retrieved BSA and GLASS BSA.

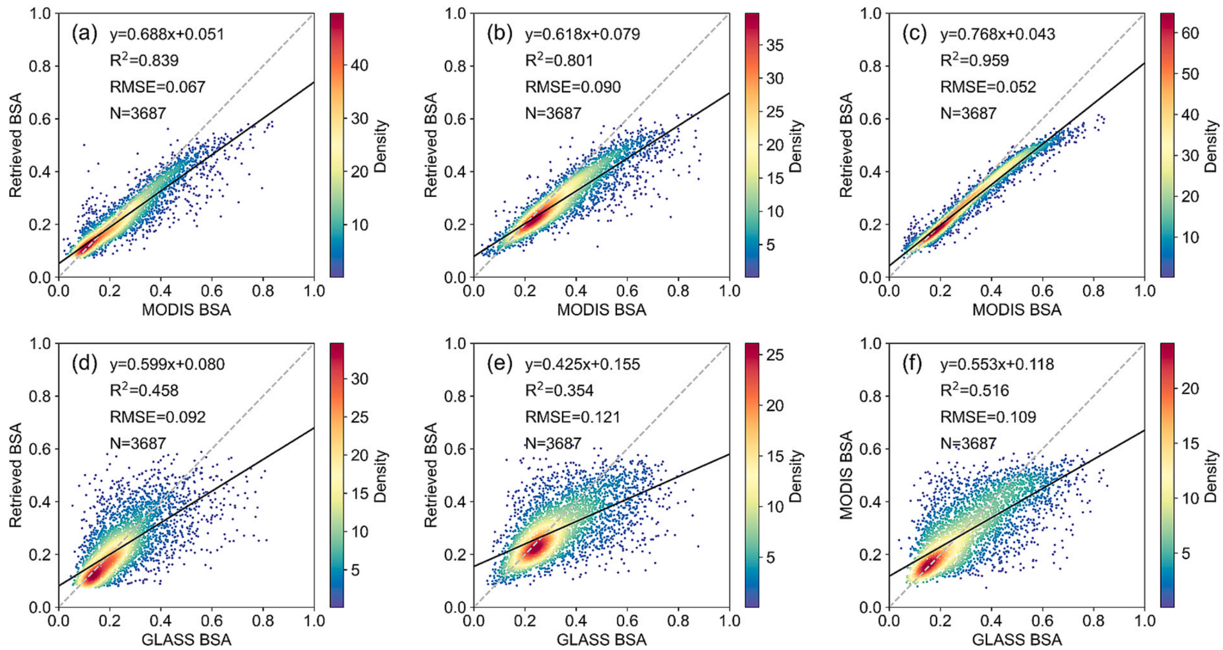

Fig. 10. Consistency of snow-covered forest albedo among the retrieved, MODIS, and GLASS products. Panels (a), (b), and (c) display comparisons between the retrieved BSA and MODIS for November 2009, January 2010, and March 2010, respectively. Panels (d), (e), and (f) show comparisons between the retrieved BSA and GLASS for the same months.

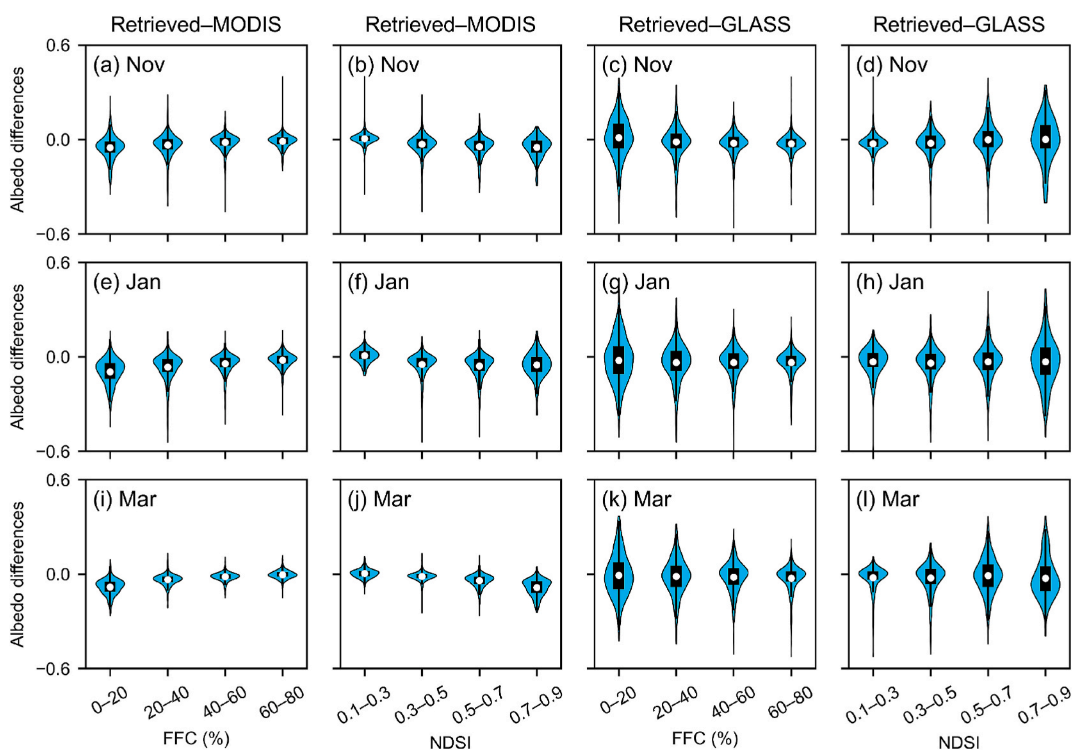

Fig. 11. Differences in snow-covered forest albedo among the retrieved, MODIS, and GLASS products. Panels (a), (e), and (i) show the differences between the retrieved BSA and the MODIS product against varying fractional forest cover (FFC) for November 2009, January 2010, and March 2010. Panels (b), (f), and (j) show the differences against varying NDSI for the same months. Similarly, panels (c), (g), and (k) show the differences between the retrieved BSA and the GLASS product based on varying fractional forest cover, while panels (d), (h), and (l) show the differences against varying NDSI.

5. Discussion

5.1. Advantages and limitations of the retrieval framework

A novel retrieval framework combining the SFBR2 radiative transfer model and machine learning has been developed for estimating snow-covered forest albedo. In this study, the SFBR2 model is extended to sloped terrain to more accurately simulate snow-covered forest reflectance under complex topographic conditions. Compared to the flat-based GORT (Wang et al., 2022; Xin et al., 2012) and SFBR2 (Chen

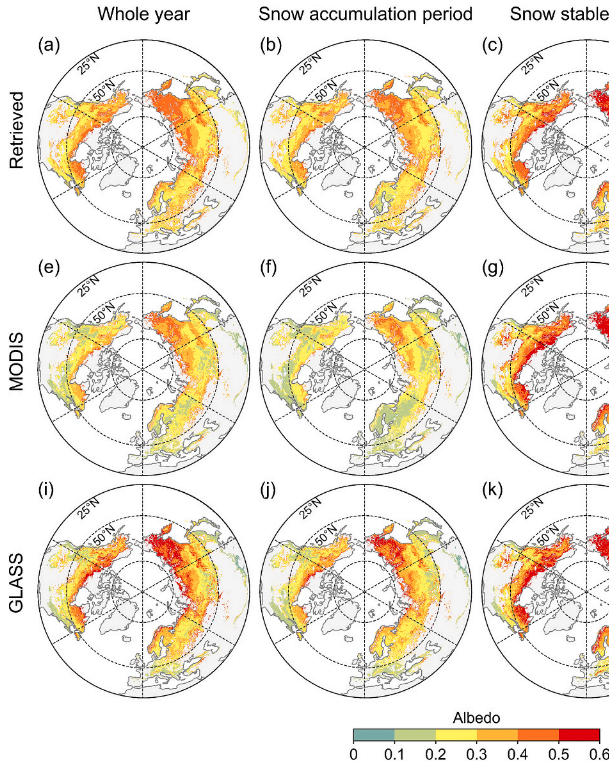

Fig. 12. Spatial patterns of snow-covered forest albedo during the whole year, snow accumulation period (September–October–November), snow stable period (December–January–February), and snow melt period (March–April–May) from 2001 to 2022.

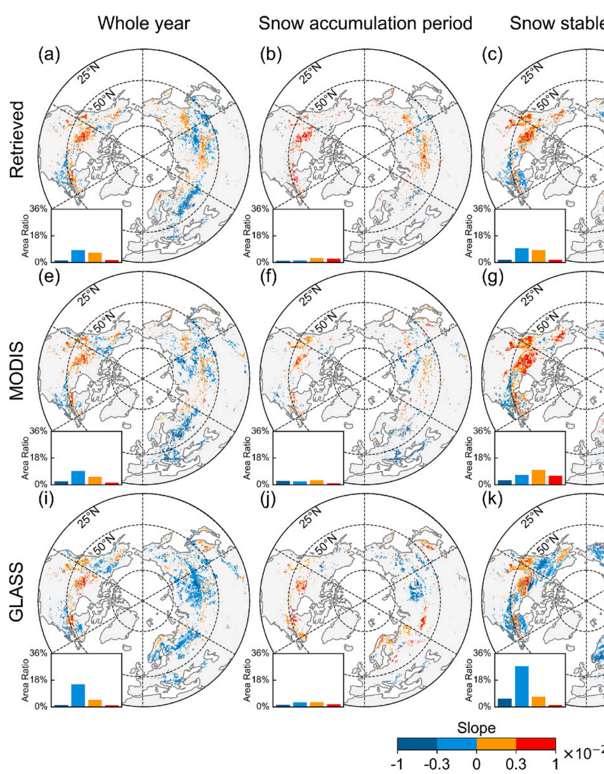

Fig. 13. Trend of snow-covered forest albedo from 2001 to 2022. The bar chart illustrates the ratio of significant change areas to the total area of snow-covered forests.

et al., 2024) models, this enhancement incorporates canopy gravitropism and corrects the area ratios of the four scene components. Thus, the retrieved snow-covered forest albedo achieves an increase in R^2 by 0.112 and a reduction in RMSE by 0.009 compared to flat terrain. For creating training datasets, previous studies often generated input features and target variables directly via radiative transfer models, such as

PROSAIL for LAI retrieval (Danner et al., 2021; Estevez et al., 2022), discrete anisotropic radiative transfer model for snow-free albedo estimation (Ma et al., 2022), and LibRadtran for solar radiation prediction (Lu et al., 2023), which may leading to unrealistic angle combinations that do not align with actual satellite observations. To address this issue, we combined real satellite reflectance observations with SFBR2-retrieved albedo, enhancing the accuracy and representativeness of the training datasets. Finally, our framework achieves higher albedo accuracy than the MODIS and GLASS products. This is because the kernel-driven model (Lucht et al., 2000) is based on a soil-canopy scene and assumes that land surface types remain constant over a period of 16 days, which does not align with the rapid changes in snow cover. On the other hand, the direct estimation algorithm (Liang et al., 2013; Qu et al., 2014) builds a training dataset based on the kernel-driven model and ART snow model, but it struggles to establish an effective mapping between snow-covered forest reflectance and albedo. Meanwhile, we employed a Random Forest model on the GEE platform to address the efficiency challenges in the retrieval process, which avoids the excessive time consumption associated with optimization algorithms such as Shuffled Complex Evolution (Shi et al., 2016; Zhang et al., 2022a), Ensemble Kalman Filter (Ma et al., 2021; Ma et al., 2017), and numerical methods (Yang et al., 2020), enabling the efficient generation of long-term snow-covered forest albedo products without the need for data downloads, mosaicking, projection, or other preprocessing steps.

However, several challenges and limitations still need to be addressed in future efforts: (1) There are some uncertainties in the cloud and snow masks. The similar spectral characteristics of clouds and snow result in an overestimation of MODIS cloud mask products in winter (Stillinger et al., 2019). Additionally, snow-covered forests are often underestimated when an NDSI threshold of 0.4 is used (Wang et al., 2020). In the MOD10A1 V6 snow product, the NDSI threshold is set to 0.1 to enhance snow identification (Riggs et al., 2015); however, there is still significant potential to enhance the accuracy of snow-covered forest mapping. (2) In generating training datasets with an optimization algorithm based on MODIS reflectance, insensitive parameters in the forward model are assigned default values, while key parameters are designated as free parameters for optimization. As fractional forest and snow cover products improve, the optimization algorithm could be further refined by assimilating these products to enhance the accuracy of snow-covered forest albedo estimation. (3) We endeavor to collect representative field data for albedo validation, considering snow-covered forest conditions, surface homogeneity, solar zenith angle limits, and clear-sky conditions. This ensures the reliability of the validation data. The consistency of results across different stations and time periods enhances the robustness of our findings. However, only nine stations for snow-covered forests are available for albedo validation, and there is a lack of effective validation data in high-latitude regions. Therefore, achieving a more comprehensive assessment remains necessary. Drone observations (Webster and Jonas, 2018) and high-resolution albedo data (Wu et al., 2020) could serve as valuable tools for assessing snow-covered forest albedo in the future.

5.2. Potential applications of snow-covered forest albedo products

In winter, snow-covered forests are widely distributed across the middle-to-high latitudes of the Northern Hemisphere. This region has undergone significant changes in recent decades, including vegetation greening (Berner and Goetz, 2022) and reduced snow cover (Bormann et al., 2018). Consequently, accurately retrieving snow-covered forest albedo and understanding its temporal and spatial variation patterns are crucial. Based on the newly generated albedo products for the Northern Hemisphere from 2001 to 2022, the variation patterns of snow-covered forest albedo across different snow periods can be effectively illustrated (Fig. 12 and Fig. 13). Furthermore, the IPCC noted that since the industrial revolution, the albedo of ice and snow has caused significant changes in radiative forcing (IPCC, 2023). Therefore, quantifying the radiative forcing and albedo feedback of snow-covered forests via our new products is an important context for assessing the Earth's energy balance. In addition, the generated snow-covered forest albedo products can serve as vital input data for ecological, climate, and meteorological models. By incorporating precise albedo products, these models can more effectively predict the impacts of albedo changes on carbon cycling, forest health, and weather forecasting. Ultimately, this contributes to more informed decision-making in environmental management and policy.

6. Conclusions

This study proposes an innovative retrieval framework for snow-covered forest albedo, in which the radiative-transfer-based retrieval method is optimized through machine learning, enabling efficient large-scale processing on the GEE platform. The training dataset is initially generated via an optimization algorithm that estimates snow-covered forest albedo from representative MODIS sample points, leveraging the well-established SFBR2 model. The trained Random Forest model is subsequently employed to retrieve snow-covered forest albedo from MODIS surface reflectance data, facilitating the rapid generation of daily products for the Northern Hemisphere on the GEE platform. According to the flux validation, our new albedo products achieved superior accuracy ($R^2 \geq 0.775$ and RMSE ≤ 0.037) in snow-covered forests compared with the MODIS and GLASS albedo products, and the consistency of our products with the MODIS albedo products is higher than that with the GLASS products. Moreover, snow-covered forest albedo in the Northern Hemisphere from 2001 to 2022 is generated and has great potential for assessing radiative forcing, ecological effects, and climate change.

CRediT authorship contribution statement

Siyong Chen: Writing – original draft, Validation, Methodology. **Pengfeng Xiao:** Writing – review & editing, Supervision, Resources, Funding acquisition. **Xueliang Zhang:** Writing – review & editing, Supervision, Funding acquisition. **Petri Pellikka:** Writing – review & editing. **Hao Liu:** Writing – review & editing. **Yantao Liu:** Writing – review & editing.

Declaration of competing interest

The authors declare that they have no known competing financial interests or personal relationships that could have appeared to influence the work reported in this paper.

Acknowledgements

This work was funded by the National Natural Science Foundation of China (Grant Nos. 42171307 and 42471410) and the AI & AI for Science Project of Nanjing University (Grant No. 020914380141). We are grateful to the High-Performance Computing Center, Nanjing University, for computational support.

References

Ali, A.M., Darvishzadeh, R., Skidmore, A., Gara, T.W., Heurich, M., 2020. Machine learning methods' performance in radiative transfer model inversion to retrieve plant traits from Sentinel-2 data of a mixed mountain forest. Int. J. Digital Earth 14 (1), 106–120.

Alibakhshi, S., Naimi, B., Hovi, A., Crowther, T.W., Rautiainen, M., 2020. Quantitative analysis of the links between forest structure and land surface albedo on a global scale. Remote Sens, Environ, p. 246.

Bair, E.H., Stillinger, T., Dozier, J., 2021. Snow property inversion from remote rensing (SPIReS): a generalized multispectral unmixing approach with examples from MODIS and Landsat 8 OLI. IEEE Trans. Geosci. Remote Sens. 59 (9), 7270–7284.

Bao, F., Huang, K., Wu, S., 2023. The retrieval of aerosol optical properties based on a random forest machine learning approach: Exploration of geostationary satellite images. Remote Sens, Environ, p. 286.

Bartlett, P.A., Verseghy, D.L., 2015. Modified treatment of intercepted snow improves the simulated forest albedo in the Canadian Land Surface Scheme. Hydrol. Process. 29 (14), 3208–3226.
Berner, L.T., Goetz, S.J., 2022. Satellite observations document trends consistent with a boreal forest biome shift. Glob. Chang. Biol. 28 (10), 3275–3292.
Bormann, K.J., Brown, R.D., Derksen, C., Painter, T.H., 2018. Estimating snow-cover trends from space. Nat. Clim. Chang. 8 (11), 923–927.
Bright, R.M., Bogren, W., Bernier, P., Astrup, R., 2016. Carbon-equivalent metrics for albedo changes in land management contexts: relevance of the time dimension. Ecol. Appl. 26 (6), 1868–1880.
Brutel-Vuilmet, C., Menegoz, M., Krinner, G., 2013. An analysis of present and future seasonal Northern Hemisphere land snow cover simulated by CMIP5 coupled climate models. Cryosphere 7 (1), 67–80.
CCI, E.L.C., 2017. Product user guide version 2.0. UCL-Geomatics: London, UK.
Cescatti, A., Marcolla, B., Santhana Vannan, S.K., Pan, J.Y., Román, M.O., Yang, X., Ciais, P., Cook, R.B., Law, B.E., Matteucci, G., Migliavacca, M., Moors, E., Richardson, A.D., Seufert, G., Schaaf, C.B., 2012. Intercomparison of MODIS albedo retrievals and in situ measurements across the global FLUXNET network. Remote Sens. Environ. 121, 323–334.
Chen, S., Xiao, P., Zhang, X., Liu, H., Wang, Y., Sun, L., Yin, G., 2024. Improved Snow-Covered Forest Bidirectional Reflectance Model Incorporating Canopy-Intercepted Snow and Atmospheric Effects. IEEE Trans. Geosci. Remote Sens. 62, 1–17.
Chen, X., Liang, S., Cao, Y., He, T., Wang, D., 2015. Observed contrast changes in snow cover phenology in northern middle and high latitudes from 2001–2014. Sci. Rep. 5 (1).
Danner, M., Berger, K., Wocher, M., Mauser, W., Hank, T., 2021. Efficient RTM-based training of machine learning regression algorithms to quantify biophysical & biochemical traits of agricultural crops. ISPRS J. Photogramm. Remote Sens. 173, 278–296.
DiMiceli, C., Carroll, M., Sohlberg, R., Kim, D.-H., Kelly, M., Townshend, J., 2015. MOD44B MODIS/Terra vegetation continuous fields yearly L3 global 250m SIN grid V006. NASA EOSDIS Land Processes DAAC 10.
Estevez, J., Salinero-Delgado, M., Berger, K., Pipia, L., Rivera-Caicedo, J.P., Wocher, M., Reyes-Munoz, P., Tagliabue, G., Boschetti, M., Verrelst, J., 2022. Gaussian processes retrieval of crop traits in Google Earth Engine based on Sentinel-2 top-of-atmosphere data. Remote Sens. Environ. 273, 112958.
Estévez, J., Vicent, J., Rivera-Caicedo, J.P., Morcillo-Pallarés, P., Vuolo, F., Sabater, N., Camps-Valls, G., Moreno, J., Verrelst, J., 2020. Gaussian processes retrieval of LAI from Sentinel-2 top-of-atmosphere radiance data. ISPRS J. Photogramm. Remote Sens. 167, 289–304.
Fernandez-Guisuraga, J.M., Verrelst, J., Calvo, L., Suarez-Seoane, S., 2021. Hybrid inversion of radiative transfer models based on high spatial resolution satellite reflectance data improves fractional vegetation cover retrieval in heterogeneous ecological systems after fire. Remote Sens Environ 255.
Hamed, K.H., Rao, A.R., 1998. A modified Mann-Kendall trend test for autocorrelated data. J. Hydrol. 204 (1).
Hao, D., Wen, J., Xiao, Q., Lin, X., You, D., Tang, Y., Liu, Q., Zhang, S., 2019. Sensitivity of Coarse-Scale Snow-Free Land Surface Shortwave Albedo to Topography. J. Geophys. Res. Atmos. 124 (16), 9028–9045.
He, T., Liang, S., Wang, D., Cao, Y., Gao, F., Yu, Y., Feng, M., 2018. Evaluating land surface albedo estimation from Landsat MSS, TM, ETM +, and OLI data based on the unified direct estimation approach. Remote Sens. Environ. 204, 181–196.
IPCC (2023). The Earth's Energy Budget, Climate Feedbacks and Climate Sensitivity. *Climate Change 2021 – The Physical Science Basis* (pp. 923-1054).
Jacquemoud, S., Verhoef, W., Baret, F., Bacour, C., Zarco-Tejada, P.J., Asner, G.P., François, C., Ustin, S.L., 2009. PROSPECT+SAIL models: a review of use for vegetation characterization. Remote Sens. Environ. 113, S56–S66.
Jeff, D., James, F., 1990. Rapid calculation of terrain parameters for radiation modeling from digital elevation data. IEEE Trans. Geosci. Remote Sens. 28 (5).
Jiao, Z., Ding, A., Kokhanovsky, A., Schaaf, C., Bréon, F.-M., Dong, Y., Wang, Z., Liu, Y., Zhang, X., Yin, S., Cui, L., Mei, L., Chang, Y., 2019a. Development of a snow kernel to better model the anisotropic reflectance of pure snow in a kernel-driven BRDF model framework. Remote Sens. Environ. 221, 198–209.
Jiao, Z.H., Ren, H., Mu, X., Zhao, J., Wang, T., Dong, J., 2019b. Evaluation of four sky view factor algorithms using digital surface and elevation model data. Earth & Space Science. 6 (2), 222–237.
Klein, A.G., Hall, D.K., Riggs, G.A., 1998. Improving snow cover mapping in forests through the use of a canopy reflectance model. Hydrol. Process. 12 (10–11), 1723–1744.
Kokhanovsky, A., Rozanov, V.V., Aoki, T., Odermatt, D., Brockmann, C., Krüger, O., Bouvet, M., Drusch, M., Hori, M., 2011. Sizing snow grains using backscattered solar light. Int. J. Remote Sens. 32 (22), 6975–7008.
Kokhanovsky, A.A., Aoki, T., Hachikubo, A., Hori, M., Zege, E.P., 2005. Reflective properties of natural snow: approximate asymptotic theory versus in situ measurements. IEEE Trans. Geosci. Remote Sens. 43 (7), 1529–1535.
Kristensen, J.Å., Barbero-Palacios, L., Barrio, I.C., Jacobsen, I.B.D., Kerby, J.T., López-Blanco, E., Malhi, Y., Le Moullec, M., Mueller, C.W., Post, E., Raundrup, K., Macias-Fauria, M., 2024. Tree planting is no climate solution at northern high latitudes. Nat. Geosci. 17 (11), 1087–1092.
Leblanc, S.G., Chen, J.M., 2000. A windows graphic user interface (GUI) for the five-scale model for fast BRDF simulations. Remote Sens. Rev. 19 (1–4), 293–305.
Lewis, P., Guanter, L., Lopez Saldana, G., Muller, J.-P., Watson, G., Shane, N., Kennedy, T., Fisher, J., Domenech, C., Preusker, R., North, P., Heckel, A., Danne, O., Krämer, U., Zühlke, M., Fomferra, N., Brockmann, C., Schaaf, C., 2012. In: The ESA globAlbedo Project: Algorithm. Place, pp. 5745–5748.
Li, Y., Zhao, M., Motesharrei, S., Mu, Q., Kalnay, E., Li, S., 2015. Local cooling and warming effects of forests based on satellite observations. Nat. Commun. 6 (1), 6603.
Liang, S., Zhao, X., Liu, S., Yuan, W., Cheng, X., Xiao, Z., Zhang, X., Liu, Q., Cheng, J., Tang, H., Qu, Y., Bo, Y., Qu, Y., Ren, H., Yu, K., Townshend, J., 2013. A long-term Global LAnd Surface Satellite (GLASS) data-set for environmental studies. Int. J. Digital Earth 6 (sup1), 5–33.
Liu, B.Y.H., Jordan, R.C., 1960. The Interrelationship and Characteristic distribution of Direct, Diffuse and Total Solar Radiation. Sol. Energy 4 (3), 1–19.
Liu, Q., Wang, L., Qu, Y., Liu, N., Liu, S., Tang, H., Liang, S., 2013. Preliminary evaluation of the long-term GLASS albedo product. Int. J. Digital Earth 6 (sup1), 69–95.
Loranty, M.M., Berner, L.T., Goetz, S.J., Jin, Y., Randerson, J.T., 2014. Vegetation controls on northern high latitude snow-albedo feedback: observations and CMIP5 model simulations. Glob. Chang. Biol. 20 (2), 594–606.
Lu, Y., Wang, L., Zhu, C., Zou, L., Zhang, M., Feng, L., Cao, Q., 2023. Predicting surface solar radiation using a hybrid radiative Transfer–Machine learning model. Renew. Sustain. Energy Rev. 173.
Luan, W., Zhang, X., Xiao, P., Wang, H., Chen, S., 2022. Binary and Fractional MODIS Snow Cover Mapping Boosted by Machine Learning and big Landsat Data. IEEE Trans. Geosci. Remote Sens. 60, 1–14.
Lucht, W., Schaaf, C.B., Strahler, A.H., 2000. An algorithm for the retrieval of albedo from space using semiempirical BRDF models. IEEE Trans. Geosci. Remote Sens. 38 (2), 977–998.
Lundberg, S., Lee, S.I., 2017. A Unified Approach to Interpreting Model Predictions.
Ma, H., Liang, S., Shi, H., Zhang, Y., 2021. An Optimization Approach for estimating Multiple Land Surface and Atmospheric Variables from the Geostationary Advanced Himawari Imager Top-of-Atmosphere Observations. IEEE Trans. Geosci. Remote Sens. 59 (4), 2888–2908.
Ma, H., Liang, S., Xiao, Z., Shi, H., 2017. Simultaneous inversion of multiple land surface parameters from MODIS optical–thermal observations. ISPRS J. Photogramm. Remote Sens. 128, 240–254.
Ma, Y., He, T., Liang, S., Wen, J., Gastellu-Etchegorry, J.-P., Chen, J., Ding, A., Feng, S., 2022. Landsat snow-free surface albedo estimation over sloping terrain: Algorithm development and evaluation. IEEE Trans. Geosci. Remote Sens. 1.
Manninen, T., Stenberg, P., 2009. Simulation of the effect of snow covered forest floor on the total forest albedo. Agric. For. Meteorol. 149 (2), 303–319.
Mousivand, A., Verhoef, W., Menenti, M., Gorte, B., 2015. Modeling top of atmosphere radiance over heterogeneous non-lambertian rugged terrain. Remote Sens. 7 (6), 8019–8044.
Muñoz Sabater, J. 2019. ERA5-Land monthly averaged data from 1981 to present, Copernicus Climate Change Service (C3S) Climate Data Store (CDS). In. Place.
Nilson, T., Kuusk, A., 1989. A reflectance model for the homogeneous plant canopy and its inversion. Remote Sens. Environ. 27, 157–167.
Niu, C., Woodgate, W., Phinn, S.R., Roelfsema, C.M., Su, Y., 2022. Extending a canopy reflectance model for mangroves: a case study in south east queensland. Australia. Agric. for. Meteorol. 316, 108875.
Pulliainen, J., Luojus, K., Derksen, C., Mudryk, L., Lemmetyinen, J., Salminen, M., Ikonen, J., Takala, M., Cohen, J., Smolander, T., Norberg, J., 2020. Patterns and trends of Northern Hemisphere snow mass from 1980 to 2018. Nature 581 (7808), 294–298.
Pulliainen, J., Salminen, M., Heinila, K., Cohen, J., Hannula, H.R., 2014. Semi-empirical modeling of the scene reflectance of snow-covered boreal forest: Validation with airborne spectrometer and LIDAR observations. Remote Sens. Environ. 155, 303–311.
Qu, Y., Liang, S., Liu, Q., He, T., Liu, S., Li, X., 2015. Mapping Surface Broadband Albedo from Satellite Observations: a Review of Literatures on Algorithms and Products. Remote Sens. 7 (1), 990–1020.
Qu, Y., Liu, Q., Liang, S., Wang, L., Liu, N., Liu, S., 2014. Direct-estimation algorithm for mapping daily land-surface broadband albedo from MODIS data. IEEE Trans. Geosci. Remote Sens. 52 (2), 907–919.
Riggs, G.A., Hall, D.K., Román, M.O., 2015. MODIS snow products collection 6 user guide. National Snow and Ice Data Center: Boulder, CO, USA 66, 545.
Rosema, A., Verhoef, W., Noorbergen, H., Borgesius, J.J., 1992. A new forest light interaction model in support of forest monitoring. Remote Sens. Environ. 42 (1), 23–41.
Rutter, N., Essery, R., Pomeroy, J., Altimir, N., Andreadis, K., Baker, I., Barr, A., Bartlett, P., Boone, A., Deng, H., Douville, H., Dutra, E., Elder, K., Ellis, C., Feng, X., Gelfan, A., Goodbody, A., Gusev, Y., Gustafsson, D., Hellström, R., Hirabayashi, Y., Hirota, T., Jonas, T., Koren, V., Kuragina, A., Lettenmaier, D., Li, W.-P., Luce, C., Martin, E., Nasonova, O., Pumpanen, J., Pyles, R.D., Samuelsson, P., Sandells, M., Schädler, G., Shmakin, A., Smirnova, T.G., Stähli, M., Stöckli, R., Strasser, U., Su, H., Suzuki, K., Takata, K., Tanaka, K., Thompson, E., Vesala, T., Viterbo, P., Wiltshire, A., Xia, K., Xue, Y., Yamazaki, T., 2009. Evaluation of forest snow processes models (SnowMIP2). J. Geophys. Res. 114 (D6).
Saltelli, A., Tarantola, S., Chan, K., 1999. Global Sensitivity Analysis of Model output a Quantitative Model-Independent Method for Global Sensitivity Analysis of Model output. Technometrics 41 (1), 39–56.
Schaaf, C.B., Gao, F., Strahler, A.H., Lucht, W., Li, X., Tsang, T., Strugnell, N.C., Zhang, X., Jin, Y., Muller, J.P., 2002. First operational BRDF, albedo nadir reflectance products from MODIS. Remote Sens. Environ. 83 (1–2), 135–148.
Sen, Kumar, P., 1968. Estimates of the Regression Coefficient based on Kendall's Tau. Publ. Am. Stat. Assoc. 63 (324), 1379–1389.
Shi, H., Xiao, Z., 2021. The 4SAILT model: an improved 4SAIL canopy radiative transfer model for sloping terrain. IEEE Trans. Geosci. Remote Sens. 59 (7), 5515–5525.

Shi, H., Xiao, Z., Liang, S., Zhang, X., 2016. Consistent estimation of multiple parameters from MODIS top of atmosphere reflectance data using a coupled soil-canopy-atmosphere radiative transfer model. Remote Sens. Environ. 184, 40–57.

Shi, H., Xiao, Z., Tian, X., 2019. Exploration of Machine Learning Techniques in Emulating a coupled Soil–Canopy–Atmosphere Radiative transfer Model for Multi-Parameter Estimation from Satellite Observations. IEEE Trans. Geosci. Remote Sens. 57 (11), 8522–8533.

Stillinger, T., Roberts, D.A., Collar, N.M., Dozier, J., 2019. Cloud Masking for Landsat 8 and MODIS Terra over Snow-Covered Terrain: Error Analysis and Spectral Similarity between Snow and Cloud. Water Resour. Res. 55 (7), 6169–6184.

Stokes, G.M., Schwartz, S.E., 1994. The Atmospheric Radiation Measurement (ARM) program: Programmatic background and design of the cloud and radiation test bed. Bull. Am. Meteorol. Soc. 75 (7), 1201–1222.

Stroeve, J., Box, J.E., Gao, F., Liang, S.L., Nolin, A., Schaaf, C., 2005. Accuracy assessment of the MODIS 16-day albedo product for snow: comparisons with Greenland in situ measurements. Remote Sens. Environ. 94 (1), 46–60.

Tachikawa, T., Hato, M., Kaku, M., Iwasaki, A., 2011. Characteristics of ASTER GDEM version 2. In: *2011 IEEE International Geoscience and Remote Sensing Symposium*. IEEE, Place IEEE, pp. 3657–3660.

Thackeray, C.W., Fletcher, C.G., Derksen, C., 2015. Quantifying the skill of CMIP5 models in simulating seasonal albedo and snow cover evolution. J. Geophys. Res.-Atmos. 120 (12), 5831–5849.

Verhoef, W., Bach, H., 2007. Coupled soil-leaf-canopy and atmosphere radiative transfer modeling to simulate hyperspectral multi-angular surface reflectance and TOA radiance data. Remote Sens. Environ. 109 (2), 166–182.

Verhoef, W., Jia, L., Xiao, Q., Su, Z., 2007. Unified optical-thermal four-stream radiative transfer theory for homogeneous vegetation canopies. IEEE Trans. Geosci. Remote Sens. 45 (6), 1808–1822.

Vermote, E.F., Kotchenova, S.Y., Ray, J.P., 2008. MODIS Surface Reflectance User's Guide.

Verrelst, J., Rivera, J.P., Veroustraete, F., Muñoz-Marí, J., Clevers, J.G.P.W., Camps-Valls, G., Moreno, J., 2015. Experimental Sentinel-2 LAI estimation using parametric, non-parametric and physical retrieval methods – a comparison. ISPRS J. Photogramm. Remote Sens. 108, 260–272.

Vikhamar, D., Solberg, R., 2003. Snow-cover mapping in forests by constrained linear spectral unmixing of MODIS data. Remote Sens. Environ. 88 (3), 309–323.

Walthall, C.L., Norman, J.M., Welles, J.M., Campbell, G., Blad, B.L., 1985. Simple equation to approximate the bidirectional reflectance from vegetative canopies and bare soil surfaces. Appl. Opt. 24 (3), 383–387.

Wang, G., Jiang, L., Xiong, C., Zhang, Y., 2022. Characterization of NDSI Variation: Implications for Snow Cover Mapping. IEEE Trans. Geosci. Remote Sens. 60, 1–18.

Wang, Q., Shi, J., 2020. Global Ecological and Environmental Remote Sensing monitoring Report 2019. Surveying and Mapping Press.

Wang, X., Chen, S., Wang, J., 2020. An adaptive snow identification algorithm in the forests of Northeast China. IEEE J. Sel. Top. Appl. Earth Obs. Remote Sens. 99, 1.

Wang, Z.S., Schaaf, C.B., Chopping, M.J., Strahler, A.H., Wang, J.D., Roman, M.O., Rocha, A.V., Woodcock, C.E., Shuai, Y.M., 2012. Evaluation of Moderate-resolution Imaging Spectroradiometer (MODIS) snow albedo product (MCD43A) over tundra. Remote Sens. Environ. 117, 264–280.

Webster, C., Jonas, T., 2018. Influence of canopy shading and snow coverage on effective albedo in a snow-dominated evergreen needleleaf forest. Remote Sens. Environ. 214, 48–58.

Weiser, U., Olefs, M., Schöner, W., Weyss, G., Hynek, B., 2016. Correction of broadband snow albedo measurements affected by unknown slope and sensor tilts. Cryosphere 10 (2), 775–790.

Wu, S., Wen, J., Lin, X., Hao, D., You, D., Xiao, Q., Liu, Q., Yin, T., 2018. Modeling discrete forest anisotropic reflectance over a sloped surface with an extended GOMS and SAIL model. IEEE Trans. Geosci. Remote Sens. 57 (2), 944–957.

Wu, X., Wen, J., Xiao, Q., You, D., 2020. Upscaling of Single-Site-based Measurements for Validation of Long-Term Coarse-Pixel Albedo Products. IEEE Trans. Geosci. Remote Sens. 58 (5), 3411–3425.

Wu, Y., Xiao, P., Zhang, X., Liu, H., Dong, Y., Feng, L., 2023. Effects of snow cover on spring vegetation phenology vary with temperature gradient across the Pan-Arctic. J. Geophys. Res. Biogeosci. 128 (4).

Xie, J., Wang, C., Ma, D., Chen, R., Xie, Q., Xu, B., Zhao, W., Yin, G., 2022. Generating Spatiotemporally Continuous Grassland Aboveground Biomass on the Tibetan Plateau through PROSAIL Model Inversion on Google Earth Engine. IEEE Trans. Geosci. Remote Sens. 60, 1–10.

Xin, Q., Woodcock, C.E., Liu, J., Tan, B., Melloh, R.A., Davis, R.E., 2012. View angle effects on MODIS snow mapping in forests. Remote Sens. Environ. 118, 50–59.

Yang, P., van der Tol, C., Yin, T., Verhoef, W., 2020. The SPART model: a soil-plant-atmosphere radiative transfer model for satellite measurements in the solar spectrum. Remote Sens. Environ. 247, 111870.

Zhang, G., Liang, S., Ma, H., He, T., Yin, G., Xu, J., Liu, X., Zhang, Y., 2024. Simultaneous estimation of five temporally regular land variables at seven spatial resolutions from seven satellite data using a multi-scale and multi-depth convolutional neural network. Remote Sens. Environ., p. 301

Zhang, G., Ma, H., Liang, S., 2022a. Estimating 250-m land surface and atmospheric variables from MERSI top-of-atmosphere reflectance. IEEE Trans. Geosci. Remote Sens. 60, 1–16.

Zhang, G., Ma, H., Liang, S., Jia, A., He, T., Wang, D., 2022b. A machine learning method trained by radiative transfer model inversion for generating seven global land and atmospheric estimates from VIIRS top-of-atmosphere observations. Remote Sens. Environ., p. 279

Zhong, X., Zhang, T., Kang, S., Wang, J., 2021. Spatiotemporal variability of snow cover timing and duration over the Eurasian continent during 1966–2012. Sci. Total Environ., p. 750